New Imaging Technologies to Enhance the Molecular Sensitivity of Positron Emission Tomography

New scintillation and semiconductor crystal detector design concepts, high density readout electronics, signal processing algorithms, and high performance computing technologies show promise to facilitate earlier detection of molecular-based disease.

By Craig S. Levin

ABSTRACT | Positron emission tomography (PET) is used in the clinic and *in vivo* small animal research to study certain molecular processes associated with diseases such as cancer, heart disease, and neurological disorders and guide the discovery and development of new treatments. New PET molecular probes and associated small animal imaging assays are under development to target, visualize, and quantify subtle molecular and cellular processes such as protein–protein interactions in signal transduction pathways, cancer cell trafficking, therapeutic stem cells and their progeny, interaction of the immune system and tumor cells, and gene delivery and expression in living animals. These next-generation PET molecular imaging assays require an order of magnitude increase in PET's ability to detect, visualize, and quantify low concentrations of probe interacting with its target, which we will refer to as *molecular sensitivity*, in order to study the subtle signatures associated with these molecular processes. The molecular sensitivity is determined by a combination of the probe and biological/physiological properties of the subject that determine its specificity for the target, and the performance capabilities of the imaging system that determine how well the resulting signal can be measured. This paper focuses on the second aspect: the challenges of advancing PET technology and some of the new imaging system technologies under investigation to substantially enhance PET's molecular sensitivity. If successful, these novel imaging system technology advances, together with new probe molecules that target specific molecular processes associated with disease, will substantially enhance the molecular sensitivity of PET and thus increase its role in preclinical and clinical research as well as evaluating and managing disease in the clinic.

KEYWORDS | Contrast resolution; image reconstruction; molecular imaging; photon sensitivity; positron emission tomography (PET); readout electronics; scintillation detectors; semiconductor detectors; spatial resolution

I. INTRODUCTION

A. Brief Overview of PET and Molecular Sensitivity

Positron emission tomography (PET) is being used in the clinic and in small animal research to noninvasively study the molecular bases of disease and to guide the development of novel molecular-based treatments. Several new molecular probes labeled with positron emitting radionuclides and associated PET imaging assays are under development to target, detect, visualize, and quantify various extra- and intracellular molecules and processes associated with diseases such as cancer, heart disease, and neurological disorders [1]–[12]. Examples of important new molecular targets and processes to study and monitor in live animal models of disease using small animal PET are protein–protein interactions in signal transduction pathways [13], [14]; cell trafficking as cancer cells metastasize to different organs [15],

[16]; therapeutic stem cells and their progeny [17], [18]; interaction of the immune system and tumor cells over time [19]–[21]; gene delivery and expression in living animals to optimize the delivery of a specific gene to a chosen target [22]–[26]; and low levels of endogenous messenger ribonucleic acid (mRNA) [27], [28].

Do currently available small animal PET systems[1] have the "sensitivity" to detect the subtle signatures associated with these molecular targets and processes? We define the *molecular sensitivity* of a molecular imaging modality as its capability to detect, visualize, and accurately quantify low concentrations of molecular probe interacting with a molecular target on or within cells of a living subject. The molecular sensitivity is defined by a combination of the probe and biological/physiological properties of the subject that determine its specificity for the target and the performance capabilities of the imaging system that determine how well the resulting signal can be detected and measured. This paper discusses the challenges of developing and further improving PET imaging technology and in particular focuses on new imaging instrumentation and algorithm approaches we are studying to substantially enhance the photon sensitivity, spatial resolution, and contrast resolution of small animal PET in order to increase its molecular sensitivity. These system enhancements will be used in conjunction with new probe molecules that target specific molecular processes associated with disease in order to advance the molecular imaging capabilities of small animal PET.

B. Definitions of Terms Used for PET in This Summary

In this paper, we will use the term *coincidence photon detection efficiency*, or simply *photon sensitivity*, to refer to the fraction of positron emission events where both 511 keV annihilation photons emitted are detected simultaneously on opposite sides of the PET detector gantry. This photon sensitivity is often quoted for a point positron source placed at the system center. High photon sensitivity enables high statistical quality of acquired data, which is required to realize the system spatial resolution potential in the reconstructed images [29]. The photon sensitivity is a product of the *geometric efficiency*, or the probability that emitted coincident photons will traverse detector material and the *intrinsic detection efficiency*, which is the probability that the two coincident photons traversing detector material will be absorbed and detected within the set energy and coincidence time windows. The term *signal-to-noise ratio* (SNR) will be used in three contexts, the first related to detector signal formation, to refer to the ratio of the electrical signal generated by the desired photon interactions to the device noise, which will impact energy,

temporal, and spatial resolution as well as photon sensitivity in PET. The second context is in regards to image analysis, to refer to the statistical quality of PET image data, and the third as a figure of merit of the true signal compared to background events produced by undesired coincidence data.

In PET, each photon detector signal from every pair coincidence event is processed individually for spatial, energy, and arrival time information. In PET, there are good events and background events. *True coincidences,* also known as *trues,* are the good coincident photon events that we want in PET data, where the line between the two photon interactions recorded on either side of the system essentially passes through their point of emission. *Random coincidences,* often called *randoms,* are a source of undesirable background counts that occur when two distinct nuclei each decay nearly at the same time and only one photon from each decay is detected within the system coincidence time window setting. Randoms rates are reduced with lower detected single photon count rates *(singles)* and a narrower coincidence time window setting. Note that it is desirable to have excellent coincidence time resolution so that a narrow coincidence time window setting during data acquisition may be employed to reject randoms without compromising photon sensitivity.

Scatter coincidences are another undesirable source of background events that occur when one or both annihilation photons emitted from the same nucleus or single photons emitted from two separate nuclei undergo one or more Compton scatter interactions in the tissue before detection. Since scatter causes a photon to lose energy, its effects may be substantially reduced through the use of a very narrow energy window setting around the 511 keV photopeak. Thus, it is also desirable to have excellent energy resolution so that a narrow energy window setting may be employed to reject scattered singles and coincidences without compromising photon sensitivity.

A figure of merit of SNR is the *noise equivalent count rate* (NECR), which is defined as the ratio of the square of the true count rate to the total count rate (trues + scatters + randoms) [30]. In PET systems where the random rate is estimated from measurements and subtracted, there is a factor of two in front of the randoms term due to error propagation [30].

Random and scatter coincidences produce a background haze of mispositioned events in the images, which degrades *image contrast and contrast resolution*, or the ability to perceive subtle probe concentration in the target from the background or subtle concentration differences between adjacent regions, respectively. The background coincidence events also reduce *quantitative accuracy*, or the ability to accurately quantify and recover the true probe concentration from the reconstructed image data. The photon sensitivity, spatial resolution, and contrast resolution work together to determine a PET system's *molecular sensitivity*, or the overall ability of the PET system to detect,

---

[1]For example, small animal PET systems from Siemens Preclinical Solutions, Inc., Knoxville, TN; GE-Suinsa, Madrid, Spain; Philips Medical Systems, Andover, MA; Oxford Positron Systems, Oxford, U.K.; Gamma Medica-Ideas, Northridge, CA; and Advanced Molecular Imaging, Quebec, Canada.

visualize, and quantify a low concentration of a molecular probe labeled with a positron emitting radionuclide accumulated within a target molecule residing within the diseased cells of a living subject.

C. How Does One Estimate the Molecular Sensitivity of PET?

To estimate the molecular sensitivity of PET, we consider a volume of positron emitting molecular probe introduced into the body, a fraction of which reaches its molecular target within the diseased cells of a living subject lying in a PET system. Assume the resulting PET data have high statistical quality and include noiseless data corrections (e.g., photon attenuation and randoms). One must estimate if it is possible from region-of-interest (ROI) image analysis to statistically distinguish the counts from probe accumulating in its molecular target from nonspecific probe signal accumulating in surrounding normal cells as well as from background photon counts. This capability relies in a complex manner on properties of the probe, the subject physiology/biology, and the imaging system. One can use the following formula to estimate the approximate ratio ρ of decays observed in the target volume (from background + target) divided by the number of decays in a background region of the same volume = [(background + target)/background = 1 + (target/background)]:

$$\rho = 1 + \frac{n \cdot N \cdot f \cdot V_t \cdot S \cdot k \cdot t \cdot P}{N_a \cdot B} \qquad (1)$$

where n = cell concentration (in cells/milliliter); N = number of copies of the target molecule per cell; f = fraction of PET probe molecules that interact (e.g., bind or react) with target molecules; V_t = target volume selected in the image data (in milliliters); S = the probe specific activity at the time the study commences (in Ci/mole), $k = 3.7 \times 10^{10}$ decays/s/Ci. We assume that during the scan, each event is decay corrected by time-stamp, or a dynamic decay correction is applied every few minutes; t = the acquisition time (in seconds); P = PET system photon sensitivity (fraction of coincident photons pairs that are detected by system); N_a = Avogadro's number; B = measured background activity in a volume equal to V_t (in Ci); and a density of 1.0 g/ml is assumed.

It is clear from (1) that the probe, the biology, and the PET instrument strongly affect the available molecular sensitivity. In the second term of the equation, the combined factor that multiplies the $1/B$ factor corresponds to the measured rate of decays resulting from just the probe accumulated in the target. Knowing this number and B, one can determine if it is statistically possible to distinguish the target from the background. A common

definition of "statistically significant" signal in comparison to the random variation in background count rate σ_B recorded during the same acquisition time is that there is a signal counting rate increase of at least $3\sigma_B$. Since B is the average background rate recorded during a time interval t, the average number of counts recorded during that time is $C = B \cdot t$, with random error $\sqrt{C}$, assuming Poisson statistics. Thus, the uncertainty in B is $\sigma_B = (1/t)\sqrt{C} = \sqrt{(C/t^2)} = \sqrt{(B/t)}$. Thus, the minimum "detectable" signal activity from the molecular target is approximately $3\sqrt{(B/t)}$. So clearly it is critical to reduce the background count rate recorded in the ROI and increase the study duration as much as possible. If desired, this minimum detectable activity can be converted to minimum detectable moles or molar concentration (mole/liter) using some of the parameters listed in (1), with a typical result of 10^{-11}–10^{-12} mol/l for PET as listed in Table 1, assuming typical target to background ratios and measured background levels for standard PET tracers.

The PET instrument performance impacts the ratio ρ through the terms V_t, P, and B of (1). Background counts are assessed from ROI image analysis. It is desired to use as small of an ROI as possible to reduce the background count level, but not so small that it cuts good signal counts. A PET system with higher reconstructed spatial resolution allows one to visualize and quantify smaller target volumes V_t before the partial volume effect reduces contrast between signal and background levels in ROI analysis. Note that V_t and B are highly interdependent since increasing the ROI used will effectively increase V_t in (1) but will also increase B, and thus will likely not improve and may even degrade ρ. A PET system with higher photon sensitivity P allows more signal counts in a given counting time, enabling higher reconstructed spatial resolution, and thus better statistics to be collected from a smaller ROI volume. Finally, a PET system with lower background counts from scatter and random coincidences will allow better contrast between signal and background for visualization of lower concentrations of probe reaching its target. Note that typically nonspecific probe targeting also contributes substantially to the total measured background signal B.

Note that higher photon sensitivity means collecting more background as well as signal counts. Higher photon statistics also facilitates high-resolution image reconstruction [29]. Consider the case of a molecular process resulting in highly focal accumulation of signal (limited to a very small region) riding on top of a flat background. With higher resolution reconstruction, more counts from the focal signal accumulation, and less from the flat background, will be contained within a smaller ROI. So in this scenario, the signal-to-background ratio is improved by using a smaller ROI. However, since a smaller ROI contains fewer background counts, the statistical uncertainty may increase, depending on the background level, but the accuracy of quantifying the signal above background will improve.

Table 1 Properties of the Most Common Commercially Available *In Vivo* Molecular Imaging Modalities[#]

Imaging modality	Form of energy used	Spatial resolution (millimeters)	Acquisition time per frame (seconds)	Molecular probe mass required (nano-grams)	Molecular sensitivity[+] (mole/liter)	Tissue penetration depth (millimeters)	Small animal or clinical?	Molecular signal quantification capabilities	Cost (equipment and usage)
PET	Annihilation photons	1-4 (animal) 6-10 (clinical)	1-300	1-100	10^{-11}-10^{-12}	>300	Both	High	High
SPECT	Gamma rays	0.5-5 (animal) 7-15 (clinical)	60-2000	1-100	10^{-10}-10^{-11}	>300	Both	Medium-High	Medium-High
BLI	Visible to infrared light	3-10	10-300	10^3-10^6	10^{-13}-10^{-16}*	1-10	Small animal	Low-Medium	Low
FLI	Visible to infrared light	2-10	10-2000	10^3-10^6	10^{-9}-10^{-11}*	1-20	Small animal	Low-Medium	Low
MRI	Radio frequency waves	0.025-0.1 (animal) 0.2-1 (clinical)	60-3000	10^3-10^6	10^{-3}-10^{-5}	>300	Both	Medium	High
Ultrasound	High frequency sound waves	0.05-0.5 (animal) 0.1-1 (clinical)	0.1-100	10^3-10^6	*	1-200	Both	Low	Low
CT	X-rays	0.03-0.4 (animal) 0.5-1 (clinical)	1-300	N/A	*	>300	Both	N/A	Medium-High

[#]Adapted from [37]. *Not well characterized yet. [+]The molecular probe, subject physiology and biology, as well as the imaging system's signal (e.g. photon) sensitivity, spatial resolution, and contrast resolution work together to define a modality's *molecular sensitivity* (the ability to visualize and quantify small concentrations of molecular signal). Here the molecular sensitivity is expressed as the limit of signal detection in units of mole/liter.

In this paper, we discuss efforts we are investigating to develop new PET instrumentation and signal-processing algorithms that will enhance spatial resolution, photon sensitivity, and contrast resolution with the net effect of improving ρ.

D. Properties and Capabilities of Common Imaging Modalities

Table 1 lists characteristics of the most common noninvasive, in vivo imaging modalities [31]. These modalities may be combined to enhance the information obtained in molecular imaging studies. Distinct advantages of radionuclide methods are that the probes are typically small, biologically relevant molecules, and only a relatively small probe mass is required so that imaging does not significantly perturb the biological processes under study. With calibrations, PET data have a high degree of quantitative accuracy for molecular signals emitted deep within tissue. Single photon emission computed tomography (SPECT) can simultaneously image multiple probes provided each is labeled with radionuclides that emit distinct photon energies. Bioluminescence imaging (BLI) and fluorescence imaging have the distinct strengths of relatively low cost and not requiring ionizing radiation, and the probes can be engineered to enable signal modulation depending upon the presence or absence of certain proteins. BLI achieves the highest molecular sensitivity since it does not require an external excitation source and

exploits a very specific enzyme-substrate interaction for a signal, allowing a very low background count rate. Magnetic resonance imaging (MRI) and computed tomography (CT) allow one to visualize very high-resolution morphology/ anatomical structure. MRI's morphological contrast resolution is highest in soft tissue, whereas CT's is best for bone and lung. In addition to measuring a wide range of physiological parameters, MRI also shows promise for providing molecular information using relatively higher mass quantities of probe. Ultrasound has the advantages of being widely available clinically, relatively inexpensive, and capable of acquiring real-time physiological information. Ultrasound also shows great promise for targeted molecular imaging combined with therapy. The modalities with the highest molecular sensitivity inherently record low background signal, have high signal (e.g., photon) sensitivity, and/or can visualize and quantify the signal with high spatial resolution no matter how deep the signal is emitted from the subject [see (1)].

II. APPROACHES TO IMPROVE PET SYSTEM PERFORMANCE

A. Challenges and Strategies to Enhance Spatial Resolution in PET

PET system developers (e.g., [32]–[45]) have made great progress but have not yet achieved the fundamental

spatial resolution inherent to PET. The physical spatial resolution limit is ultimately determined by a convolution of three blurring factors: positron range, annihilation photon acollinearity, and intrinsic detector resolution [46]. For central points within the tomograph field of view (FOV), the intrinsic detector resolution for two coincident detector elements is approximately one-half the detector element size. The blurring component due to positron range is shift invariant but depends upon the positron emission energy range and the tissue traversed. The photon acollinearity effect on spatial resolution depends on the system diameter. Fig. 1 shows a plot of the calculated spatial resolution [full-width at half- and tenth-maximum (FWHM) and (FWTM), respectively] for a point source of ^{18}F in water-equivalent tissue determined by these three blurring factors for various system diameters as a function of detector pixel size [46]. In principle, ~750 μm FWHM (submillimeter) resolution is attainable with 1 mm detector pixellation and $\leq$ 20 cm system diameter, provided there are adequate counts to reconstruct at that desired resolution with acceptable SNR [29]. It is clear from this figure that to increase PET spatial resolution, one should build a system with as small crystal pixels and system diameter (or distance between opposing detectors) as possible. However, there are several challenges faced by these goals that we discuss in this section.

1) Complex and Expensive Assembly: Higher spatial resolution PET data are achieved by using smaller detector
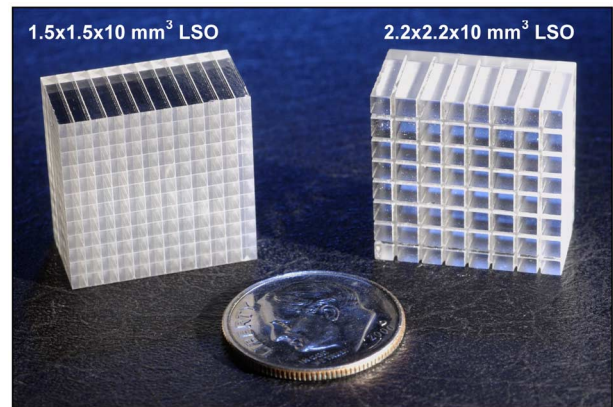

Fig. 2. *Example 8 × 8 arrays of discrete LSO scintillation crystals pixels used in two successive generations of microPET systems. In these system designs, each array is coupled to a position sensitive photomultiplier tube. (Courtesy of Siemens Preclinical Solutions.)*

elements to provide finer sampling of the biodistribution of interest. A major challenge of manufacturing PET detectors with smaller (< 2 mm wide) scintillation crystal elements is that cutting, surface treatments, and assembling crystals to make arrays (e.g., Fig. 2) are complex and expensive processes. One approach under investigation to address this issue is to use semiconductor detector crystals such as cadmium zinc telluride (CZT) [47]–[50] (e.g.,
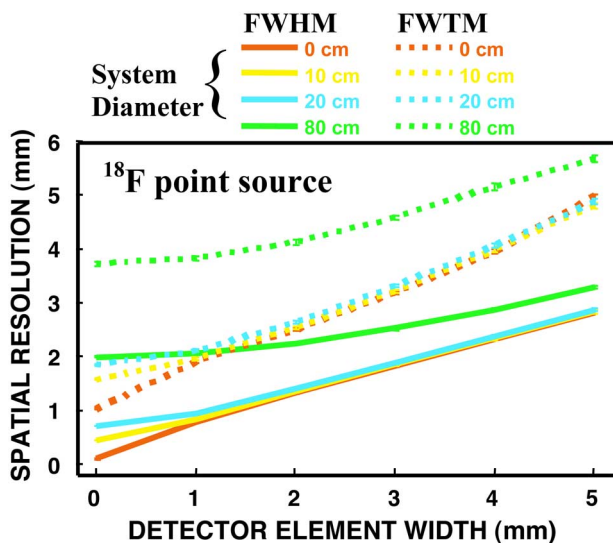
Fig. 1. *Calculated* ^{18}*F point source spatial resolution (FWHM and FWTM) limit for PET from a convolution of positron range, photon acollinearity, and detector contributions as a function of detector pixel size and the system detector diameter. In theory, for a 1 mm detector pixel and* $\leq$ *20 cm detector separation, adequate statistics, and sufficient sampling,* < *1 mm FWHM spatial resolution is possible. Adapted from [46].*
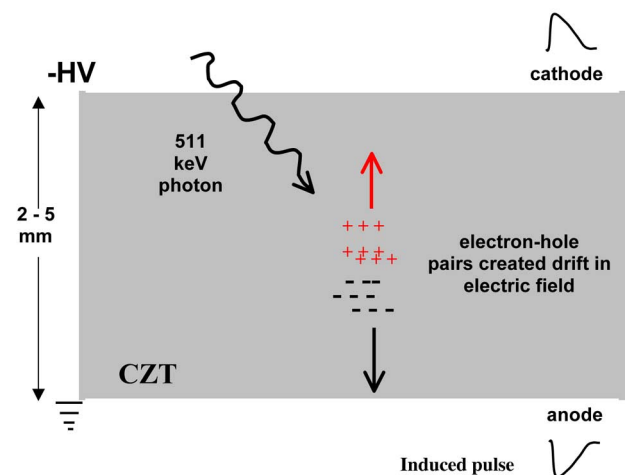
Fig. 3. *Schematic depiction of a basic direct interaction semiconductor detector. Similar to what happens in a scintillation crystal, each incoming photon enters the detector and interacts via Compton scatter or photoelectric effect, which ejects a fast electron from the crystal atoms. The recoil electron ionizes the nearby atoms creating electron-hole pairs. However, unlike a scintillation crystal, the electrons and holes drift in opposite directions in a strong electric field (e.g., ~1 kV/cm) established across the crystal. The motion of the charges induces a negative pulse on the anode and positive pulse on the cathode, each of which is integrated and processed for spatial, spectral, and/or temporal information.*

Table 2 Some Properties of CZT and Common Scintillation Crystals Used in PET

Crystal	Effective Atomic Number Z_{eff}	Density ρ (g/cm³)	1/e Length at 511 keV (cm)	Total Linear Absorption Coefficient μ at 511 keV (cm⁻¹)	Compton Scatter Fraction μ_c/μ at 511 keV (cm⁻¹)	Photoelectric Absorption Fraction μ_p/μ at 511 keV (cm⁻¹)	Average Number of Electrons* Created per MeV absorbed	Refractive Index n	Decay Time (ns)	Peak Emission Wavelength (nm)
"CZT" $Cd_{0.9}Zn_{0.1}Te$	48	5.81	2.00	0.500	0.820	0.180	200,000	N/A	N/A	N/A
"LSO" $Lu_2(SiO_4)O{:}Ce$	66	7.40	1.13	0.869	0.620	0.323	4,400	1.82	42	420
"GSO" $Gd_2(SiO_4)O{:}Ce$	59	6.71	1.40	0.704	0.700	0.249	1,400	1.85	60	440
"BGO" $Bi_4(GeO_4)_3$	75	7.13	1.06	0.966	0.510	0.397	1,200	2.15	300	480

*For LSO, GSO, and BGO a PMT photocathode quantum efficiency of 20% was assumed here and photoelectrons created at the photocathode are listed.

Fig. 3) or cadmium telluride [51] instead of scintillation crystals (see Table 2). In semiconductor crystals, a strong electric field is established across the crystal by applying a relatively large potential difference on the two electrodes (anode and cathode) on either face of a monolithic crystal slab, as depicted in Fig. 3. An incoming annihilation photon interacts with the atoms in the semiconductor crystal, just as it would in a scintillation crystal, except the electron-hole pairs created are separated, drift toward opposite faces (electrons toward the anode, holes toward the cathode), and directly detected by the device. The motion of the charge induces signals on the respective electrodes that may be used to extract spatial, energy, and temporal information. Thus, unlike scintillation crystals, semiconductor detectors directly sense the ionization signal created by the annihilation photon absorption and do not create, transport, and collect scintillation light.

In semiconductor detectors, fine spatial pixellation is set by the segmented pattern of charge-collecting electrodes deposited on the crystal slab faces, rather than relying on cutting, treating, and assembling many miniscule crystal pixels. In the most common design, the anode plane is segmented into tiny square conductors (e.g., Fig. 4), the cathode is a continuous plane, and the x-y interaction coordinate is determined by the pattern of charge induced on the anode squares. A less common design is to use a set of parallel, very thin rectangular strips across the anode and an orthogonal set on the cathode [52]. The x-y coordinate of the interaction in this case is determined by the intersection of the strips on either side of the crystal slab that record a signal above threshold. In either case, to achieve high intrinsic spatial resolution, one deposits the electrodes with a pitch that matches the desired spatial resolution (0.5 mm, for example). The advantage of the cross-strip electrode design compared to the square pixel design is that fewer electronic channels are required ($2n$ versus n^2) to achieve a given intrinsic spatial resolution.

2) Less Light Signal is Available: Of all the photon sensing fields, PET imposes perhaps the most stringent requirements on detector capabilities. The detector crystals must comprise relatively high atomic number (Z), high-density

materials for a high probability of the photoelectric effect, and high intrinsic detection efficiency of the 511 keV photons. Typically high-quality inorganic scintillation crystals are used (see Table 2). The crystals absorb the 511 keV photons and convert them into robust electronic signals, which must be processed one at a time in order to precisely determine the interation position, energy and arrival time of each incoming photon. For high detection efficiency, the crystals must also be thick (> 2 cm).
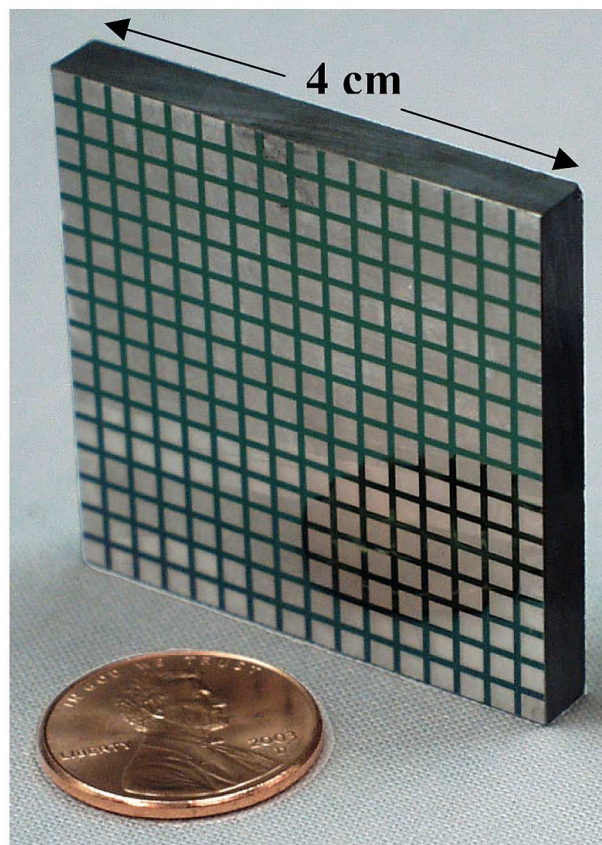

Fig. 4. *Picture of a 40 × 40 × 5 mm³ CZT array. The 256-pixel device shown has 2.25 mm anode pixels (indium) deposited on a 2.5 mm pitch. The backside has a continuous cathode.*

However, for high spatial localization of the incoming photons, a high degree of crystal segmentation/pixellation (< 2 mm) is required. This long yet very narrow aspect ratio for the individual scintillation crystal elements imposes certain challenges. With narrow crystal elements, the scintillation light collection efficiency is compromised.

Fig. 5 shows results from Monte Carlo simulations of light collection efficiency for $2 \times 2 \times 10$ and $1 \times 1 \times 10 \text{ mm}^3$ crystals, with all faces covered in a high-reflectivity diffuse white reflector except the one small end that is coupled to the photodetector [53]. The longer and narrower the crystal element, the less light collected from that end. If the resulting light signal in each crystal is above the corresponding photodetector noise level, it is possible to achieve high-resolution PET; however, it is clear this scenario is not preferred since ultimately a weak scintillation light signal negatively impacts resulting energy and temporal resolution performance (which affect energy and time window settings), and limits the degree of spatial decoding in the case of a light multiplexed crystal array design. Modest light collection improvements can be made by proper treatment of the crystal faces, such as polishing or well-controlled etching, to enhance total internal reflection (see Fig. 5). Higher crystal refractive index also generally improves the probability of total internal reflection to facilitate light collection (e.g., CsI has the lowest refractive index and BGO the highest in Fig. 5). Ground surfaces do not promote total internal reflection, and so there is less correlation of light collection efficiency with index of refraction seen in the figure.

To provide a more favorable aspect ratio with moderate light collection efficiency (somewhere between the two extremes presented in Fig. 5), ≤ 2 mm resolution PET systems built to date (e.g., [32]–[45]) use relatively short ($\sim$10 mm length) crystals (e.g., see Fig. 2). But this short crystal design severely compromises intrinsic 511 keV photon detection efficiency. For example, building a PET system with 1-cm-long lutetium oxyorthosilicate (LSO) crystals affects the intrinsic coincident photon detection efficiency by a multiplicative factor $[\varepsilon = (1 - e^{-\mu x})^2;$ $x = 1$ cm; $x = 1$ cm] of 0.34, contributing to the relatively low ($\sim$few percent) overall photon sensitivity achieved with currently available high-resolution PET systems [49].

One approach under investigation [53]–[56] to increase light collection efficiency for high-resolution scintillation crystal designs is to read out the larger area side faces of the long and narrow crystals, rather than the small area ends of the crystals (see Fig. 6), thereby substantially improving the light collection aspect ratio [53]. In this new geometry, with the photodetector plane generally "edge-on" with respect to incoming annihilation photons, the average light path to the photodetector is greatly reduced and the light collection is nearly complete (> 95%; see Fig. 7), independent of individual crystal length, width, and surface treatment, as well as origin of the scintillation light. These factors help to achieve high energy and temporal resolution in addition to high spatial resolution, without requiring special crystal surfaces or promotion of total internal reflection. In order to accomplish this feat in an array, while maintaining high crystal packing fraction, very thin semiconductor photodetectors are configured in between the crystal planes (see Fig. 8). Since the thin photodetector can be position sensitive, the annihilation photon interaction depth may
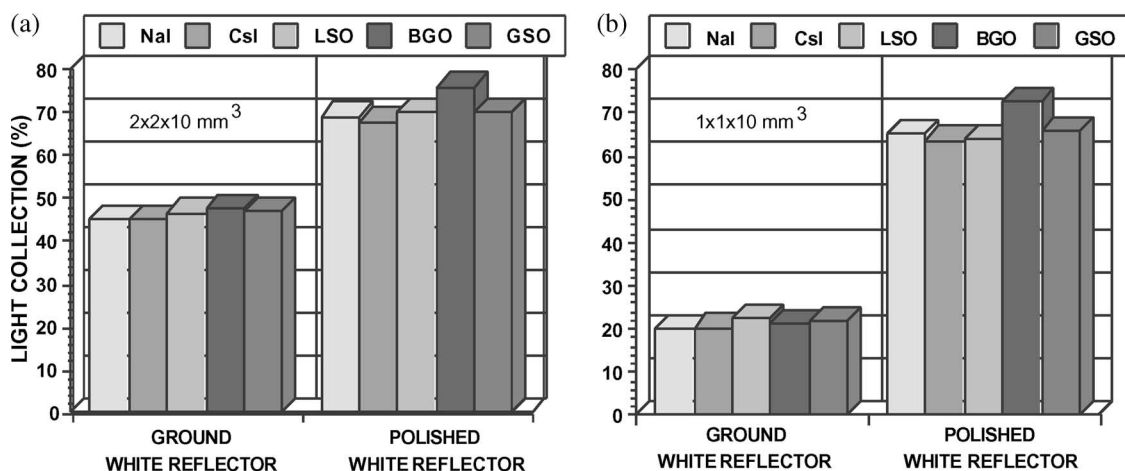
Fig. 5. *Monte Carlo simulation calculated light collection efficiency from the ends of (a) $2 \times 2 \times 10 \text{ mm}^3$ and (b) $1 \times 1 \times 10 \text{ mm}^3$ crystal rods for different scintillation crystal materials and two different surface treatments. The "polished" treatment is the ideal perfectly specular surface, which cannot be accomplished in practice, so the corresponding data represent a light collection efficiency upper limit for the end readout configuration. The "ground" or "polished" surfaces are applied to all surfaces except that coupled to the photodetector. "Ground" and "polished" surfaces means diffuse and spectral, respectively, with respect to light ray reflections. We see that attempts to go from 2×2 to $1 \times 1 \text{ mm}^2$ crystal pixel area significantly compromise light collection efficiency. Note that if intermediate fiber coupling between the crystals and photodetectors is used, the light collection efficiency will further decrease significantly.*
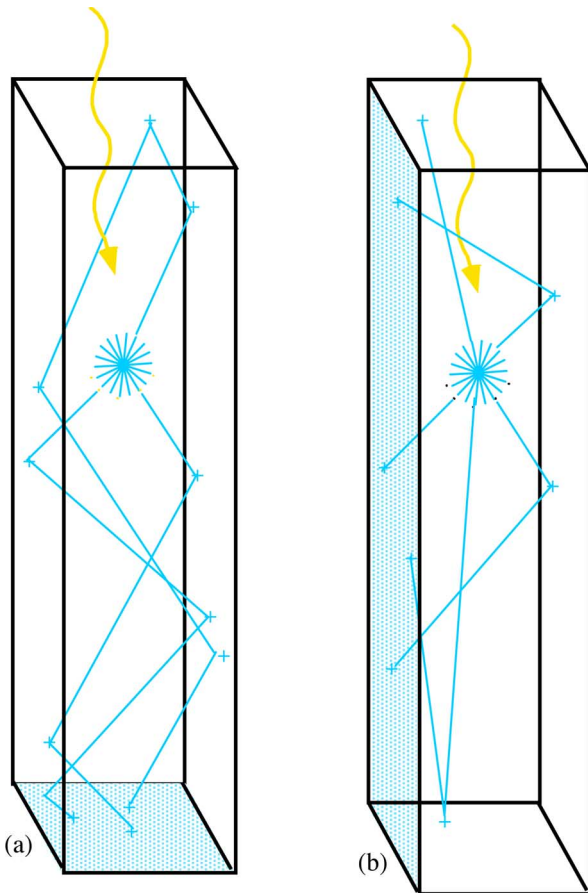
Fig. 6. *When an annihilation photon enters the crystal, a light flash is created. The paths of a few light rays are shown ("+" represents points of reflection off of the crystal surfaces) for two different scintillation light readout configurations of miniscule crystal rods used in high-resolution PET. The conventional scintillation light readout is from one small end (a), which suffers from poor light collection aspect ratio. If instead the photodetector is configured on one long side of the crystal (b), the light collection aspect ratio is much more favorable (e.g., 10 : 1 rather than 1 : 10 for a 1 × 1 × 10 mm³ crystal), facilitating nearly complete scintillation light collection.*

be directly measured as well [53], [54]. Extra thin position sensitive avalanche photodiodes (PSAPDs) have been manufactured for these purposes (Fig. 9) [55], [56].

Of course, another design strategy to altogether avoid the problem of lower light signal from small scintillation crystal elements is to use the aforementioned direct detection semiconductor detector approach [47]–[51], which directly senses the charge created from absorption of an annihilation photon (see Fig. 3) and completely avoids the pitfalls associated with creation, propagation, and collection of scintillation light in miniscule scintillation crystals.

3) Photon Penetration and Parallax Blurring Effects: Since 511 keV photons are highly penetrating, as the crystal pixels become narrower, it becomes impossible to confine

their interactions to just one crystal element. Fig. 10 shows results from Monte Carlo simulations of 511 keV photons entering obliquely (at 20° with respect to the normal) into an array of 1 × 1 × 10 mm³ LSO crystal pixels. The line of dense interactions in the array corresponds to the line of entry. For this configuration, assuming an energy threshold of 350 keV on the summed interaction energies per photon event and a lower energy cutoff of 10 keV per interaction, 84% of the detected incoming photons penetrate and deposit energy beyond the crystal of entrance. A PET system typically comprises a circular arrangement of such arrays [Fig. 11(a)]. This substantial crystal penetration leads to nonuniform spatial resolution.

For a small diameter PET system or a dual-panel system with closely spaced detectors, on average more photons will enter and be absorbed in the scintillation crystal at oblique rather normal angles for a given imaging subject. In this case, photons will tend to interact at depth in crystals behind the first crystal traversed, causing a parallax error [57]. Due to the variation of photon interaction depth within the crystals for oblique entering photons, there will be blurring of the radial component of the spatial resolution that increases with radial position [see Fig. 11(a)]. This blurring can be compensated for if one can determine the photon interaction depth.

The accuracy to which photon interaction depth can be measured, referred to as the *interaction depth resolution*, impacts the radial blurring in the following manner. Let r represent the distance from the tomograph center to a line of response (LOR) chord that corresponds to photons incident at angle θ_i that interact at the center of two isolated crystal segments of length Δd of a system of radius R [see Fig. 11(a)]

$$r = (R + (\Delta d/2)) \sin \theta_i. \qquad (2)$$

An expression for the radial resolution blurring Δr as a function of r can be determined for photons incident at angle θ_i that interact in an isolated detector with interaction depth resolution Δd by assuming that the entire length of that crystal segment Δd is uniformly radiated by these oblique photons. This radial resolution blurring for photons interacting in two isolated detectors in coincidence is approximately given by [see Fig. 11(a)]

$$\begin{aligned} \Delta r &\approx \Delta x/2 = (\Delta d/2) \sin \theta_i \quad \text{(FWHM)} \\ &= (\Delta d/2)r/[R + (\Delta d/2)] \\ &= r/[(D/\Delta d) + 1] \end{aligned} \qquad (3)$$

where D is the system diameter, which we will assume to be 8 cm for purposes of illustration. Mice and rats
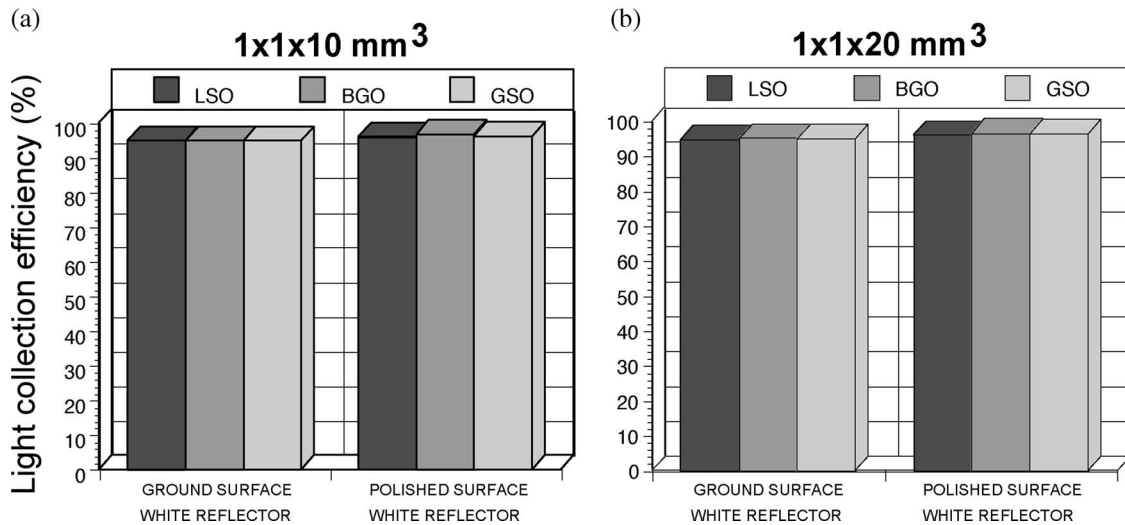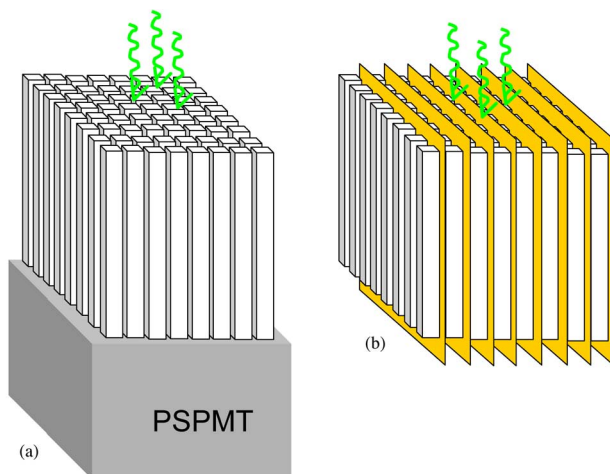
Fig. 7. *Plots of scintillation light collection efficiency reading out the sides of 1×1 mm^2 cross-sectional area crystal rods for (a) 10 and (b) 20 mm length, polished and diffuse surface treatment, and three materials. For this side readout configuration, the light collection efficiency is $>$ 95%, independent of crystal parameters and origin of light [compare with Fig. 5(b)]. Adapted from [53].*

used in most molecular imaging experiments are completely contained within a 3 cm FOV radius, which will help to limit the extent of photon depth of interaction (DOI) blurring.

Fig. 11(b) plots this radial blurring (3) as a function of radial position of a point source assuming an interaction depth resolution Δd of 2, 5, or 10 mm. For example, for a radial position $r = 1.6$ cm, on average photons are incident on an isolated detector segment $\Delta d = 5$ mm length with $\theta_i = 22°$, and from (3) the radial blurring for

interactions in that crystal segment would be $\Delta r = 0.9$ mm FWHM. At a radial position of 3 cm and with $\Delta d = 5$ mm, $\theta_i = 45°$, the corresponding $\Delta r \sim 1.7$ mm FWHM. At a radial position of 1.6 cm with $\Delta d = 10$ mm, $\Delta r = 1.8$ mm FWHM. At a radial position of 3 cm with $\Delta d = 10$ mm, $\Delta r = 3.3$ mm FWHM. To determine the radial blurring effect on overall spatial resolution, this blurring factor is convolved with the other inherent

Fig. 8. *Instead of (a) the conventional scintillation array readout geometry, the enhanced scintillation light collection configuration depicted in Fig. 6(b) is achieved (b) in an imaging array configuration using very thin semiconductor photodetectors placed in between each crystal plane.*
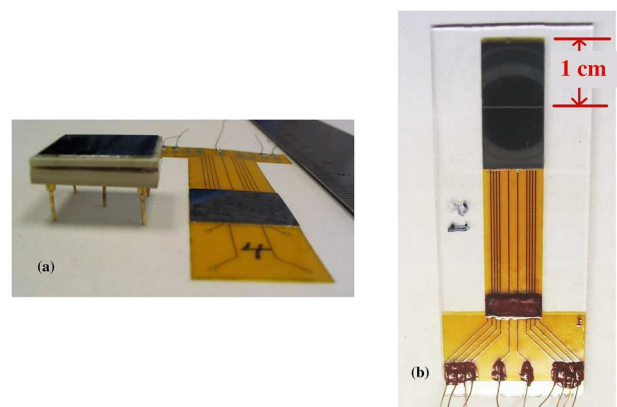

Fig. 9. *(a) Picture of the standard PSAPD device as well as the extra thin module, both manufactured at RMD, Inc. (Watertown, MA). The thin device comprises a $\sim$200-μm-thick PSAPD chip mounted on a 50-μm-thick flex circuit. The flex circuit delivers bias to each PSAPD and enables readout of the four corner signals for positioning. (b) Picture of the thin module with two PSAPD chips mounted. With an LSO array mounted to each chip, and each dual-LSO-PSAPD scintillation detector layer oriented edge-on, incoming photons encounter a minimum of $\sim$2 cm thick of LSO with directly measured photon interaction depth.*
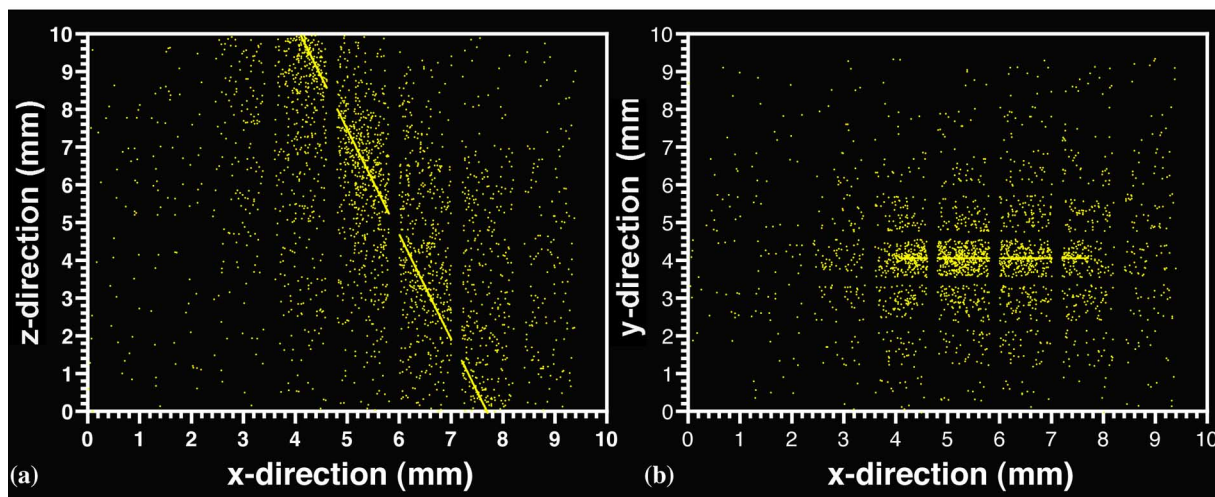
Fig. 10. *Monte Carlo simulation calculated distribution of interaction vertices in an 8 × 8 array of 1 × 1 × 10 mm³ LSO crystals for a narrow beam of 511 keV photons entering at a 20° incident angle with respect to the normal onto a center crystal. Views of the distribution projected from the (a) side and (b) top of the array are shown. A total of 20 000 incident photons were simulated. Adapted from [53].*

blurring factors [46]. For example, at a 1.6 cm radial position, including the other resolution blurring factors (see Fig. 1), the 8-cm-diameter system radial resolution prediction would be approximately 1.2 and 1.9 mm FWHM, respectively, for $\Delta d = 5$ and 10 mm, assuming adequate counts to reconstruct at the resolution depicted in the data of Fig. 1. Note that although depth resolution will help reduce DOI radial blurring effects for the full system, it is always best to position the subject as close to the system axis as possible.

Measuring annihilation photon interaction depth may be accomplished with three-dimensional (3-D) *positioning detectors,* that is, detectors that are capable of localizing the 3-D interaction coordinates of the incoming photon. For the scintillation crystal design with edge-on PSAPDs configured on the sides of miniscule LSO crystal elements [53], [54], this 3-D positioning capability may be attained by segmenting the crystal fingers into arrays [Fig. 12(a)] [53]–[56]. A measured 511 keV photon flood field image of an array with $1 \times 1 \times 3$ mm³ discrete LSO crystals is
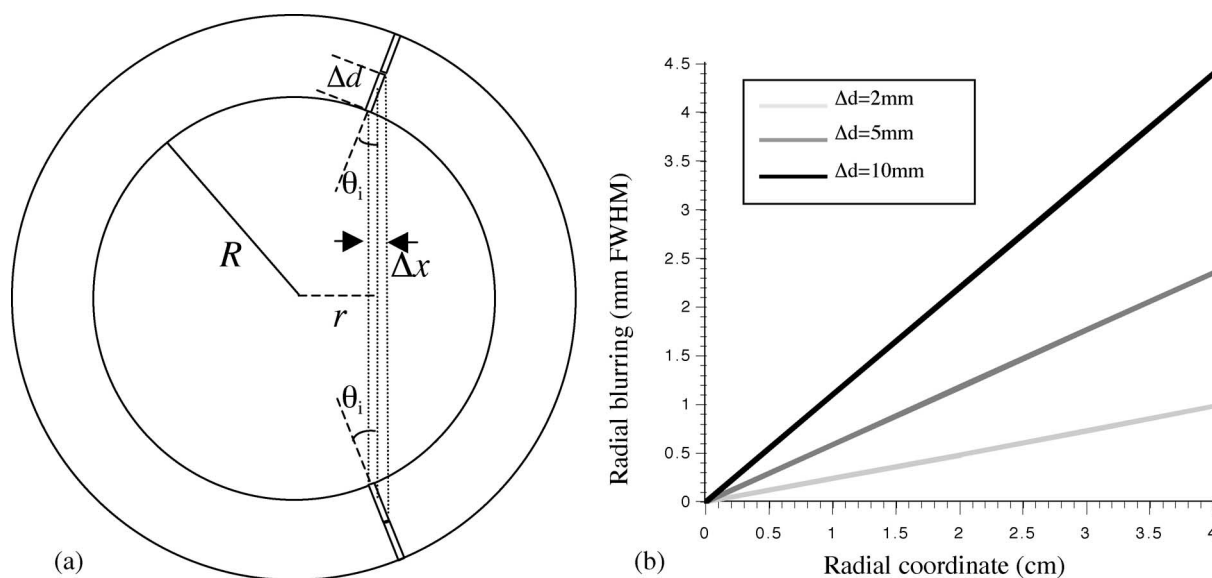
Fig. 11. *(a) Depiction of the estimated radial resolution blurring due to interaction depth variation for coincident photons emitted from a point source located at radial coordinate r, entering obliquely into two isolated crystals. (b) The estimated radial resolution blurring plotted as a function of radial position of a point source for an 8-cm-diameter PET system for different photon interaction depth resolutions.*
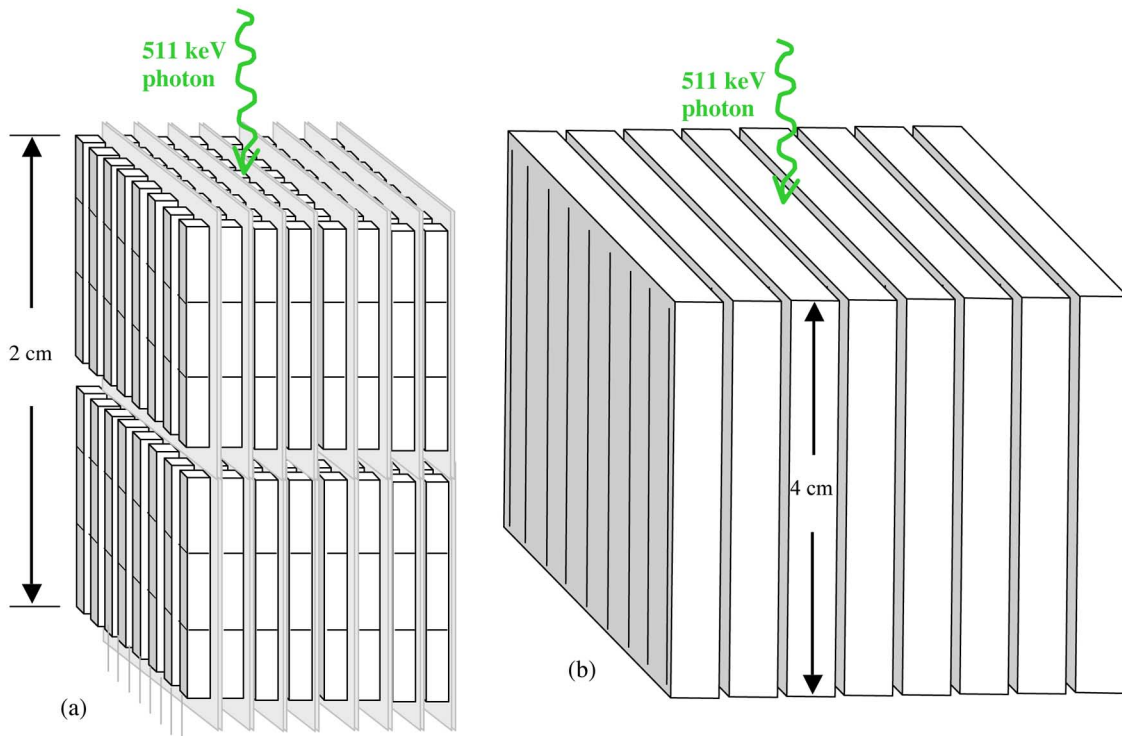
Fig. 12. *Depiction of two PET detector schemes under development that are capable of resolving the 3-D photon interaction coordinates. (a) Stacked layers of dual-LSO-PSAPD scintillation detector arrays with $1 \times 1 \times 3$ mm^3 discrete crystals. Each scintillation detector layers comprises two LSO arrays coupled to two independent PSAPD chips [see Fig. 9(b) for a picture of the PSAPD]. The LSO array/PSAPD chip combination on each of the scintillation detector layers operates independently from one another. In this arrangement, incoming photons encounter a minimum of 2-cm-thick LSO, with 3 mm directly measured depth resolution. (b) Stacked slabs of independently operating $40 \times 40 \times 5$ mm^3 cross-strip CZT detectors. In the configuration shown, photons encounter 4-cm-thick material with uniform, directly measured depth resolution determined by the cathode strip pitch on the backside of each slab (not shown). The other two interaction coordinates are determined by the anode pitch and the ratio of the cathode to anode pulse heights. In both drawings, the spaces between crystals have been exaggerated.*

shown in Fig. 13. Note that another PSAPD-based PET detector design has been studied [58]. This other design applies PSAPDs on both ends of an LSO crystal array and uses the two resulting signals to estimate the weighted mean of the interaction depth coordinate per event [58]. However, this detector design only has capabilities to estimate the weighted mean coordinates of the photon interactions per event but cannot determine whether multiple interactions occur within the array. Other researchers have developed APD-based PET detectors with [59] and without [60], [61] capabilities of estimating photon DOI.

For the cross-strip CZT design, the detectors can also be arranged edge-on [Fig. 12(b)]. As stated, in the planes parallel to the electrodes, the x-y interaction coordinate for an event recorded in any given slab is determined by the intersection of the signals recorded in the orthogonal strips. The third coordinate along the direction orthogonal to the cathode and anode plane may be determined using the ratio of the cathode to anode signal pulse heights [47], [62]. Point spread function measurements with the cross-strip detectors indicate that the

resolution along the edge (parallel to the electrodes) is precisely defined by the anode or cathode strip pitch [47], depending which direction the beam is translated, and in the cathode-to-anode direction (orthogonal to the electrodes), the intrinsic resolution is below 1 mm FWHM [47].

To study the effect of resolving the photon interaction depth in a 3-D positioning detector, we simulated a PET system built from the high-resolution $40 \times 40 \times 5$ mm^3 cross-strip CZT detectors and performed a simulated PET acquisition of a high resolution sphere phantom at several different detector resolutions along the photon interaction depth direction (the resolution of the other two coordinates was assumed to be 1 mm). Fig. 14 shows the resulting images reconstructed with the list mode 3D ordered subsets expectation maximization (OSEM) algorithm [80]. Due to the photon interaction depth resolution capability, the spatial resolution is essentially uniform all the way out the edge of the system FOV (detector aperture = useful FOV), but noticeably more uniform for the 3- compared to 5-mm depth resolution near the edges of the FOV.
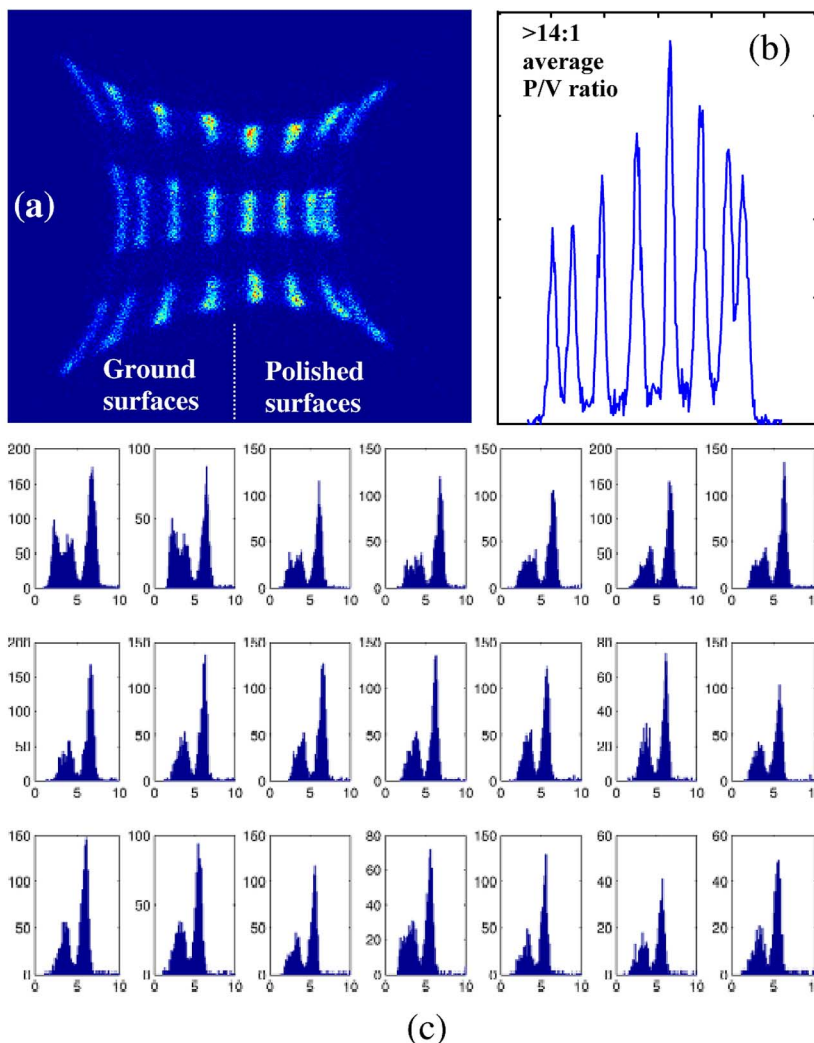
**Fig. 13.** (a) Scintillation crystal positioning histogram from flood irradiation of 511 keV photons from a point ^{22}Na source for one 8×3 array of $1 \times 1 \times 3$ mm^3 LSO crystals (without intercrystal reflector) coupled to one of the PSAPD chips shown in Fig. 9(b). This unit corresponds to one independent half of one of the scintillation detector layers depicted in Fig. 12(a). For this experiment, the left and right 12 crystals had fine ground and polished surfaces, respectively, in order to study the effect of surface treatment on crystal separation in the flood image. This image is used to develop a lookup table for assignment of crystal positions and correcting the well-known PSAPD pincushion spatial nonlinearity artifact [54]–[56]. (b) Profile through center crystal row shows that with either crystal surface treatment, the crystals are well separated in the flood histogram, with a peak-to-valley ration of $> 414 : 1$. (c) Pulse height (energy) spectra measured in each of the 24 crystals yield an average energy resolution of $10.03 \pm 4.05\%$ FWHM for the 511 keV photopeak. The edge crystals were partially off the 8×8 mm^2 sensitive PSAPD area. This excellent energy resolution enables the use of a narrow energy window setting around the photopeak to reject photons that scatter in tissue while maintaining high photopeak counts.

4) Positioning Errors From Photon Compton Scatter in Crystals: Besides photon penetration, another challenge for positioning 511 keV photons is that they often undergo Compton scatter in the crystal material. If the crystal elements are small, the scattered photons will usually escape into adjacent crystals before depositing their remaining energy. Fig. 10 shows the distribution of 511 keV photon interactions for a photon entering obliquely into an LSO array of $1 \times 1 \times 10$ mm^3 pixels; the events with one or more Compton scatter interactions

produce the energy depositions seen off the line of entrance. Mispositioned scatter events contribute to the tails of the response function (not the FWHM [106]). For an energy threshold of 350 keV on the summed interaction energies per photon event and a lower energy cutoff of 10 keV per interaction, ~25% of the detected events would be positioned away from the true line of entrance. The crystal scatter probability is higher for relatively low Z, lower density crystals such as gadolinium orthosilicate (GSO) and CZT, where on average each
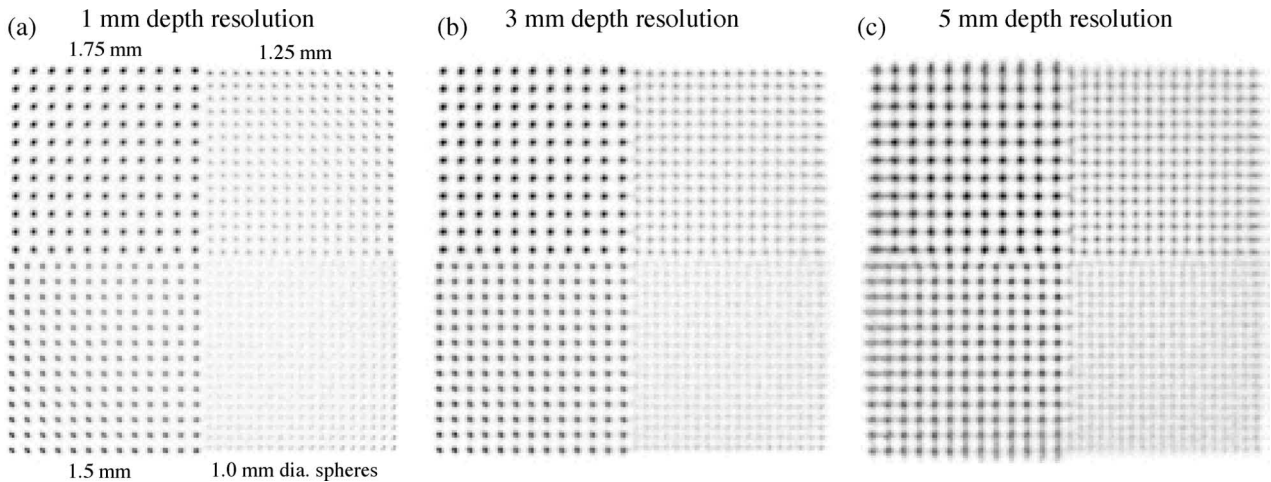
Fig. 14. *Reconstructed sphere resolution phantom (1, 1.25, 1.5, and 1.75 mm diameter with pitch equal to twice the diameter) acquired in a Monte Carlo simulated PET system (8 × 8 × 8 cm³ FOV) built with the cross-strip CZT detector design depicted in Fig. 12(b), for three different photon interaction depth resolutions (a, b, and c, respectively for 1, 3, and 5 mm cathode strip pitch). Each interaction of each incoming photon event was binned to the center of the nearest 1 × 1 × Δd mm detector voxel, where Δd is the photon interaction depth resolution, to simulate realistic detector resolution. Images were reconstructed with 20 iterations of list-mode 3-D OSEM [80]. Note that unlike most resolution phantoms, this one extends all the way out to the edge of the 8 × 8 cm transaxial FOV of the system defined by the detectors. For all three depth resolutions, the spheres are well resolved all the way out to the FOV edge (best for 1 mm depth resolution), so that the useful FOV = the detector FOV.*
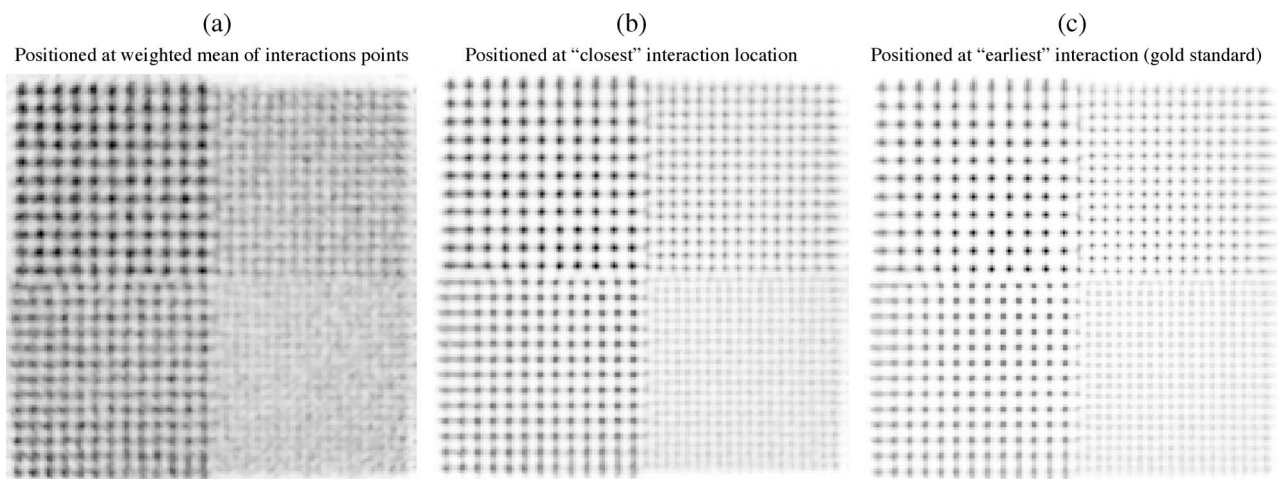
Fig. 15. *Reconstructed sphere resolution phantom (1, 1.25, 1.5, and 1.75 mm diameter with pitch equal to twice the diameter) acquired in a Monte Carlo simulated PET system (8 × 8 × 8 cm³ FOV) built with the cross-strip CZT detector design depicted in Fig. 12(b). Each interaction for every incoming photon event was binned to the center of the nearest 1 × 1 × 5 mm detector voxel. Images were reconstructed with 20 iterations of list-mode 3D OSEM. The data shown used the following multi-interaction photon positioning schemes: (a) weighted mean over all interaction locations per event; (b) location of interaction with minimum distance to the other coincident photon position; and (c) interaction that occurred earliest (ideal). Adapted from [107].*

incoming 511 keV photon produces ~2 interactions in the crystal (a scatter followed by a photoabsorption). The scatter probability is also significant in higher Z crystals such as LSO as well (see Table 2), if they are small. Crystal scatter out of small crystal elements can be a major source of event positioning error in high-resolution PET systems, which in turn can degrade

spatial resolution and contrast resolution. Crystal scatter is not as much a problem for standard clinical systems with larger (≥ 4 mm width) crystal elements, since a larger crystal is more likely to completely absorb the energy from two interactions.

The impact of crystal scatter on positioning errors can be reduced with the availability of high-resolution 3-D

position sensitive detectors. The standard position sensitive PET detector uses light multiplexing in the scintillation crystal array (e.g., [63]) and/or charge multiplexing in the position sensitive photodetector (e.g., [64]) or associated readout circuit (e.g., [65]) resulting in a few, typically four, readout channels. Such detectors have only two-dimensional (2-D) positioning capabilities; that is, they estimate the 2-D photon interaction coordinates (x-y) for each event by determining the array crystal closest to the 2-D weighted mean of the readout signals. Thus, individual interaction coordinates and their energies deposited cannot be determined in the standard PET detector. Since 3-D positioning detectors are capable of recording the 3-D coordinates and energy deposition for every interaction, it is possible to use more intelligent positioning algorithms to better estimate the line of entrance of an incoming photon in order to mitigate the effect of crystal scatter positioning errors. Such positioning algorithms may incorporate the physics of Compton scatter and/or a probabilistic formalism such as maximum likelihood to estimate the first interaction location.

Fig. 15 shows image reconstruction results from a simulated PET acquisition of the sphere resolution phantom in a PET system built from high-resolution 3-D positioning CZT detectors [107]. In these data, the coordinates of the first interaction in multi-interaction photon events were estimated using 1) the standard weighted mean positioning over all interactions and 2) a more intelligent, yet simple algorithm that estimates the interaction location closest to the weighted mean position of the other annihilation photon interactions in the system. We see that the latter algorithm, which requires a 3-D positioning detector, greatly reduces the effect of crystal scatter on resolution compared to the weighted mean approach. Also, shown for reference is the gold-standard algorithm that positions the first interaction per multi-interaction event based upon the earliest arrival time, which is ideal information that, due to real time resolution limits, is only available to Monte Carlo simulated data sets.

5) Lower Photon Flux per Crystal Element: The smaller the crystal element, the fewer photon counts placed in that crystal, and hence, the lower the SNR per crystal. Thus, in order to achieve the desired spatial resolution in terms of SNR in reconstructed images [29], the system photon sensitivity must be substantially increased. Strategies to increase the photon sensitivity are discussed in the next section.

## B. Challenges and Strategies to Enhance Photon Sensitivity in PET

This fraction should be as high as possible to achieve acceptable SNR for high spatial resolution reconstructed images. Better statistical quality of the data also enhances the ability to differentiate and quantify a subtle signal in the presence of significant background counts. The photon sensitivity is determined by the geometric efficiency, which depends on the solid angle coverage of the detector; and the intrinsic detection efficiency, which depends upon the crystal Z, density, thickness, and packing fraction as well as the energy and coincidence time window settings.

1) What is the Best Geometric Detector Arrangement?: A PET system is built from detector modules. The modules are typically rectangular in shape. Arranging rectangular-shaped detectors into a cylinder produces gaps between detectors where photons can escape [Fig. 16(a)], which lowers intrinsic detection efficency. If one considers a point source placed at the center of the system with fixed transaxial and axial FOV widths, of all possible detector geometries, arranging rectangular detectors into a four-sided polygon (i.e. a square or rectangle) provides the highest sensitivity (Fig. 17) [49]. The analytically estimated all-interactions data in Fig. 17 use only the exponential linear attenuation formula $e^{-\mu x}$, where μ = the total CZT linear attenuation coefficient at 511 keV, and do not take into account crystal scatter effects and escape of scattered photons into gaps. On the other hand, the accurate all-interactions Monte Carlo simulated data in Fig. 17 model crystal scatter effects. The analytically estimated photo-electric-only data in Fig. 17 use the same linear attenuation formula, except with the photoelectric-only linear attenuation coefficient of CZT. The fact that the two all-interaction curves diverge with increasing detector sides but the photoelectric-only data match quite well implies that the simulated all-interactions photon sensitivity trend seen in Fig. 17 is due mainly to the fact that many photons undergo crystal scatter, and the four-sided system polygon has in general a more favorable distribution of gaps to minimize crystal scatter photon escape [49]. This fact is
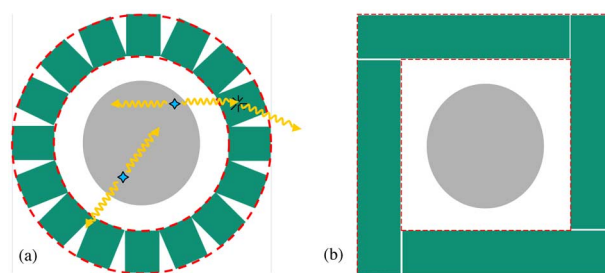
Fig. 16. *(a) The standard configuration of arranging rectangular-shaped block detectors into a cylindrical system configuration yields many intermodule wedge-shaped gaps that provide a path for photons to escape [49]. The escape of photons that have undergone scatter in the detector crystals (example shown) is more likely and plays a larger role in degrading system photon sensitivity than does the escape of photons that do not scatter in the crystal (example shown). (b) The proposed box-shaped system with corners filled enables substantial improvements in photon sensitivity (~19% using 4-cm-thick CZT) adapted from [49].*
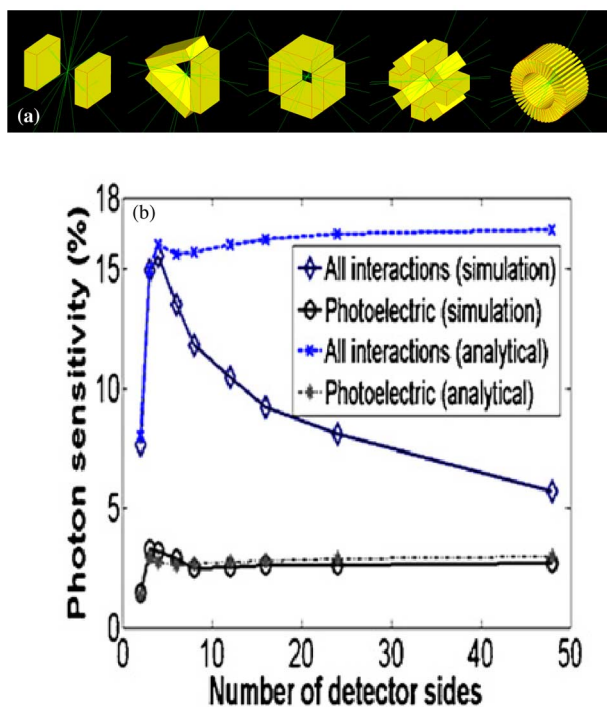
Fig. 17. *(a) Five of the nine system PET system polygon designs that were simulated to study photon sensitivity [49]. The simulated systems were all constructed from rectangular-shaped detector modules to form a fixed transaxial and axial FOV. The green lines indicate example photon trajectories. (b) Simulated and analytically estimated center point source photon sensitivity (coincident photon detection efficiency) as a function of number of sides in the system polygon for fixed $8 \times 8 \times 8$ cm^3 FOV built with $40 \times 40 \times 5$ mm^3 CZT submodules (350–650 keV energy window) [49]. The all-interactions analytically estimated data were calculated using the exponential linear attenuation formula $e^{-\mu x}$, where $\mu =$ the total CZT linear attenuation coefficient at 511 keV, and thus did not take into account crystal scatter effects and escape of scattered photons into gaps, which explains why it does not compare well with the Monte Carlo simulated all-interactions curve. The four-sided geometry provides the most favorable distribution of gaps (four corner gaps) that minimizes loss of crystal-scattered photons, yielding $> 15\%$ photon sensitivity for a point source of annihilation photons located at the center. With the corners filled [Fig. 16(b)], this number increases to $\sim$19% [49]. Note that for photon sensitivity calculations, the energy threshold applied to each photon event is on the sum energy of interactions deposited in one or more detectors. Adapted from [49].*

true for both small animal as well as clinical system geometries, although for the latter, the photon sensitivity differences between a cylindrical and rectangular geometry are reduced since the system diameter and the individual crystal pixels are larger, the gaps are relatively smaller, and so a smaller fraction of crystal scatter photons escape [49].

If the corners of the box-shaped CZT system are filled [Fig. 16(b)], a significant additional photon sensitivity boost is possible, resulting in $\sim$19% center point source photon sensitivity for a very narrow 496–526 keV energy window [49]. Note that for simulation of the photon sensitivity, the energy threshold applied to each photon event is on the sum energy of interactions deposited in one or more detectors. Another advantage of the four-sided system is that it is relatively easy to design the system to allow movable heads with selectable FOV [49] to bring the detectors closer to the subject and accommodate different size subjects. This approach enables a second additional boost in photon sensitivity by increasing geometric efficiency. Using detectors capable of measuring photon DOI, one can bring the detectors in closer together for increased photon sensitivity, and hence enhanced image SNR, while mitigating parallax errors that blur spatial resolution (Fig. 11). Of course, to further improve the geometric efficiency, along with moving the detectors closer to the subject contours, a PET system developer should incorporate as large an axial span of detectors as possible and cost-effective.

2) Crystal Length (Thickness) and Packing Fraction: Since the intrinsic coincidence photon detection efficiency for any two detector pairs varies with crystal element length l as the square of an exponential ($[\varepsilon = (1 - e^{-\mu l})^2]$), it is clear that the crystal length should be as large as possible. However, as discussed in the previous section, for the standard scintillation crystal detector design used in high-resolution PET, light collection efficiency diminishes and the crystal penetration and scatter problems increase with longer crystal pixels. The new scintillation detector under study that reads the light from the side of each crystal [Fig. 12(a)] has the same high ($> 90\%$) light collection efficiency independent of crystal length [53]. In this design, the PSAPD photodetector between crystal planes is very thin (< 300 μm) to preserve a good crystal packing fraction (fraction of area seen by incoming photons that is covered by crystal). In addition, due to the excellent light collection aspect ratio, intercrystal reflectors are unnecessary [54]–[56]. For the nonscintillating semiconductor detector design [Fig. 12(b)], light collection is not an issue and the crystals can be configured with $> 99\%$ intermodule packing fraction [47], [49].

Both the scintillation and semiconductor detectors under study can position the 3-D coordinates of photon interactions, enabling the use of relatively long (thick) crystals for high intrinsic detection efficiency while mitigating other photon penetration and scatter effects associated with thick crystals. The CZT detectors have relatively low Z and low density, and it is challenging to manufacture good quality detectors thicker than 5 mm. Thus, to achieve high detection efficiency, the 5-mm-thick detector slabs are arranged edge-on with respect to the general direction of incoming annihilation photons so that they traverse a minimum of 4-cm-thick CZT material [47]–[49]. The CdTe detector arrays that have been described to date for PET [51] comprises two layers of 1.1 mm $\times$ 5.0 mm $\times$ 1.0 mm, with effective crystal

thickness seen by incoming photons of only 1 cm. Since there is no intercrystal reflector required in this CZT design, the crystal packing fraction is potentially much higher than for pixellated scintillation crystal designs, so that fewer photons escape through gaps between crystals [49].

3) Algorithmic Approaches to Recover Single and Tissue Scatter Photons: In Section II-A, we saw that using detectors capable of estimating a third dimension of the photon absorption location and/or the 3-D coordinates of the individual interactions had benefits of 1) eliminating parallax positioning errors to facilitate uniform spatial resolution throughout the system FOV and 2) providing a more accurate estimation of the first interaction for improved photon positioning and thus reconstructed spatial resolution. There are other benefits of these 3-D-positioning capabilities. By resolving individual photon interactions in the detector, there is also an opportunity to include certain events that are normally rejected from the PET data set, thus effectively increasing photon sensitivity [66], [67]. Using more sophisticated image reconstruction algorithms that incorporate the knowledge of the energy and location of individual interactions and physics of Compton scatter, it may be possible to include 1) unpaired single photons [66], which are normally rejected by the coincidence criteria, and 2) include tissue scattered

coincidence photons [67], normally rejected by the energy window setting, into the data set without loss of spatial resolution or contrast. Depending on the system photon sensitivity, the number of single unpaired annihilation photons detected by the system can be an order of magnitude or more higher than the number of paired coincident photons, as is the case for standard clinical systems since they typically have a relatively low ratio of diameter to axial FOV. Also, the number of tissue scattered coincident photons can be substantial, especially for clinical imaging. In fact, using a very low energy threshold, tissue scatter events can be 70% of all coincident photon events [68]. Thus, if there was a method to include these normally rejected photon events into the image reconstruction process, without compromising spatial resolution and contrast, the photon sensitivity could be effectively increased by an order of magnitude or more.

Fig. 18 depicts two reconstructions of a plane through a sphere resolution phantom acquired in a system built with 3-D positioning CZT detectors. Fig. 18(a) used only data from the coincidence photon events, while Fig. 18(b) used a data set comprising both coincidence + single photons [108]. The two data sets and processing methods had different convergence properties. For the coincidence-only data, two iterations and ten subsets were used. For the coincidence plus singles data, one iteration and five

(a) Coincident photons only

(b) Singles + coincident photons
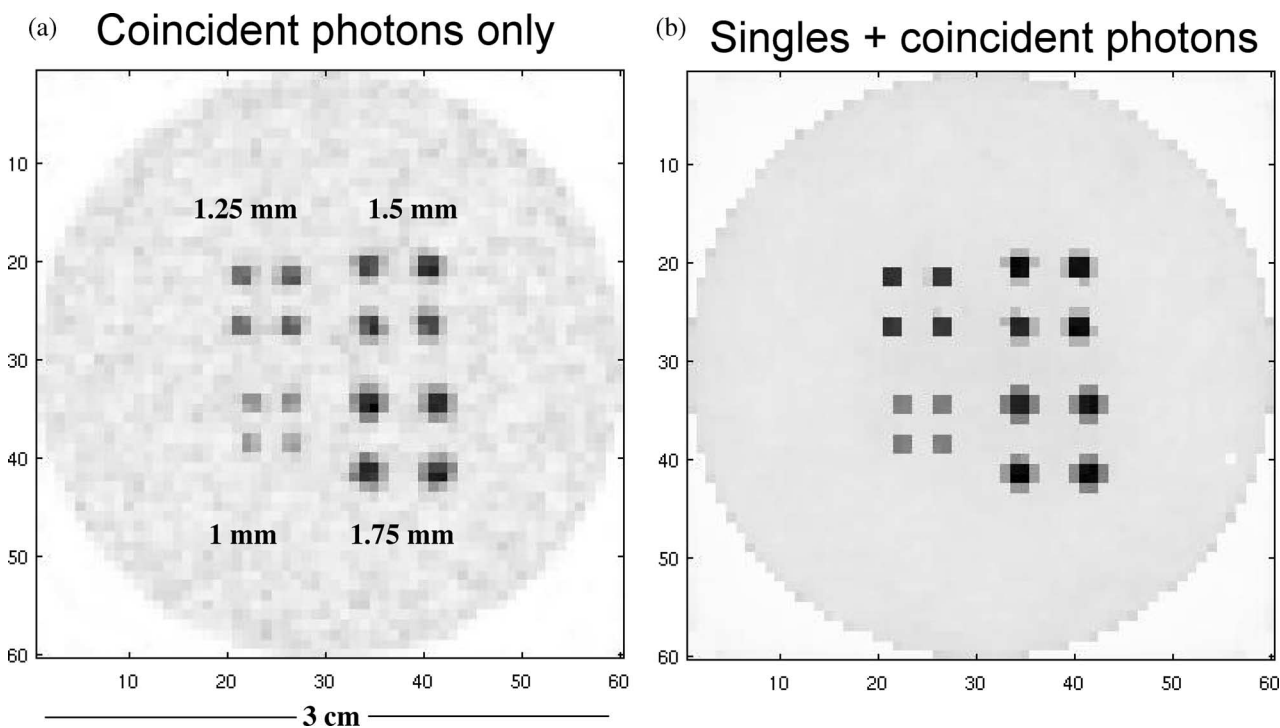
Fig. 18. *Reconstruction of simulated sphere resolution phantom data in a high resolution PET system built with 3-D positioning CZT detectors. (a) Only coincidence photon data. (b) Coincident photon data combined with single photon data that was reconstructed with a Bayesian prior defined by the reconstructed coincidence data [66]. Preliminary results indicate that the combined data have improved SNR compared to the standard coincidence only data (see Table 3). Adapted from [108].*

subsets were used. In this simulated system, the coincident photon sensitivity is high so that the number of single unpaired photon events roughly equals the number of paired coincidence photon events. In order to enable high reconstructed resolution for the single photon data, the reconstructed coincidence photon image data were used as a prior in the reconstruction of the single photon data, with a novel Bayesian projection method [66]. Preliminary data presented in Table 3 and Fig. 18 show that by effectively increasing the counts in the reconstructed data set by a factor of two, the SNR (mean/variance) was improved significantly in the latter case without compromising spatial resolution or contrast [66]. Please note that the observed improvements do not follow simple Poisson statistics based on the extra counts available by including the single photons into the data set. In addition to the two data-processing schemes having different convergence properties, the Bayesian projection method effectively produces a modification in the system of equations to be solved and so the two processing methods likely have different bias as well.

C. Challenges and Strategies to Enhance Contrast and Contrast Resolution in PET

The contrast and contrast resolution of the probe signal in a particular region of interest in images depend strongly upon the background photon coincidence signal present. This background has two main components. First, there is typically nonspecific targeting of the probe in cells surrounding the ROI. The extent of this effect depends upon the molecular probe design, physiology of the subject, and biology of the target (e.g., see [69]). Secondly, processes such as photon scatter in the tissue, random coincidences, partial volume effect, and line forward- and back-projection during image reconstruction will place counts outside the desired target volume in the image and into the surrounding background, degrading contrast and accuracy. The impact these factors have on background depends upon certain system performance parameters. Here we discuss detector system design approaches to reduce scatter and random coincidence background counts and briefly describe the benefits of time-of-flight PET on the SNR of line-projection processing in image reconstruction. The partial volume effect [70] is mitigated by designing the system to achieve high spatial resolution and so will not be further discussed here.

1) Effects of Photon Scatter: Photons that undergo scatter in the tissue before reaching the detector lose energy, depending upon the scatter angle. To mitigate this effect, an electronic pulse height lower and upper threshold (in other words, *energy window setting*) is imposed on each incoming detector signal. The effects of photon scatter on the background level can be reduced by implementing a very narrow energy window. However, if window setting is narrower than roughly a factor of twice the natural energy resolution of the system, measured at FWHM of the typical Gaussian-shaped photopeak in a measured pulse height spectrum, then the photon sensitivity will be compromised. On the other hand, if a relatively wide energy window around the 511 keV peak energy is selected (e.g., 350–650 keV), then the image data set will include a significant fraction of events where one or more photon has scattered. A detector system with excellent energy resolution allows the use of a narrow energy window setting to reject contamination from photons that have scattered while preserving high photon counts from the photopeak.

Table 3 Variance/Mean (Inverse of SNR) and Contrast Ratio for the Images Presented in Fig. 18. Adapted from [108]

ROI	Coincidence photons only		Singles + coincidence photons	
	Variance/Mean	Contrast ratio	Variance/Mean	Contrast ratio
Background	1.19±0.11	1.00	0.11 ±0.01	1.00
1 mm dia. sphere	1.46 ±0.37	4.00	0.24 ±0.06	5.17
1.25 mm dia.	0.88 ±0.22	6.36	0.53 ±0.13	8.32
1.5 mm dia.	1.24 ±0.32	7.91	1.01 ±0.26	9.33
1.75 mm dia.	0.78 ±0.20	9.31	0.46 ±0.12	9.41

Authorized licensed use limited to: Stanford University. Downloaded on May 20,2010 at 17:49:34 UTC from IEEE Xplore. Restrictions apply.

For example, consider a PET system that uses the described LSO-PSAPD scintillation detectors with $\leq 12\%$ FWHM energy resolution (see Fig. 13). With a 450–575 keV (24%) energy window centered at 511 keV, this system will have a comparable fraction of accepted events to that of a PET system, which has $\geq 25\%$ energy resolution (e.g., [64], [71], [72]) and uses a 350–650 keV (59%) energy window. However, with a 450 keV lower energy threshold, Compton scatter kinematics dictates that only photons that scatter at $\leq 30°$ are accepted into the data set. For a system that uses a 350 keV threshold, all photons that scatter $\leq 68°$ are accepted into the image data, and, compared to the former case, there will be significantly higher random and scatter contamination and thus inferior lesion contrast resolution and quantitative accuracy. One advantage of CZT is its superior energy resolution measured at < 3% FWHM at 511 keV [47]–[49] (Fig. 19). Thus, a CZT-based system would require roughly a 496–526 keV (6%) energy window centered on 511 keV for best photon sensitivity. With a 496 keV lower energy threshold, only the relatively small fraction of photons that scatter at < 14° would be accepted into the data set.

Fig. 20 shows simulation results of event rates as a function of energy window from a breast imaging phantom configuration (warm breast and torso, hot heart) acquired in a breast-dedicated PET system under development that is built with LSO-PSAPD detectors with ~12% FWHM energy resolution at 511 keV [73]. The coincidence photon scatter rate in the proposed system was reduced by a factor of three for the 24% compared to 59% energy windows

(see Fig. 20) and even a higher reduction factor results [73] when compared to a system with $\geq 25\%$ FWHM energy resolution [64], [71], [72]. The random coincidence rate in Fig. 20 drops by nearly a factor of two for 59% versus 24% energy windows [73]. The random rate depends upon energy window setting since single photons that undergo scatter can contribute to the random coincidence rate. So a system with superior energy resolution can help to mitigate the effect of random coincidences in addition to scatter coincidences.

2) Effects of Random Coincidences: Random coincidences can also be a significant source of background counts and contribute to degrading contrast and less accurate quantification. For a PET system with random coincidence background rates, R_{ij} measured along any given line of response (LOR) between any two crystal elements i and j with recorded single photon rates S_i and S_j, respectively, the rate of this background source may be estimated by the equation $R_{ij} = 2\Delta t S_i S_j$, where Δt is the coincidence time window setting. Thus, to reduce the effects of background, the time window should be as narrow as possible and the single photon rates recorded throughout the system as low as possible. Analogous to the case for the energy window, if the coincidence time resolution is excellent, the coincidence time window setting can be narrow (but approximately twice the coincidence time resolution) without degrading photon sensitivity. We have achieved 2 ns FWHM coincidence time resolution with LSO-PSAPD detectors [54], [55], so for photon sensitivity, a 4 ns setting
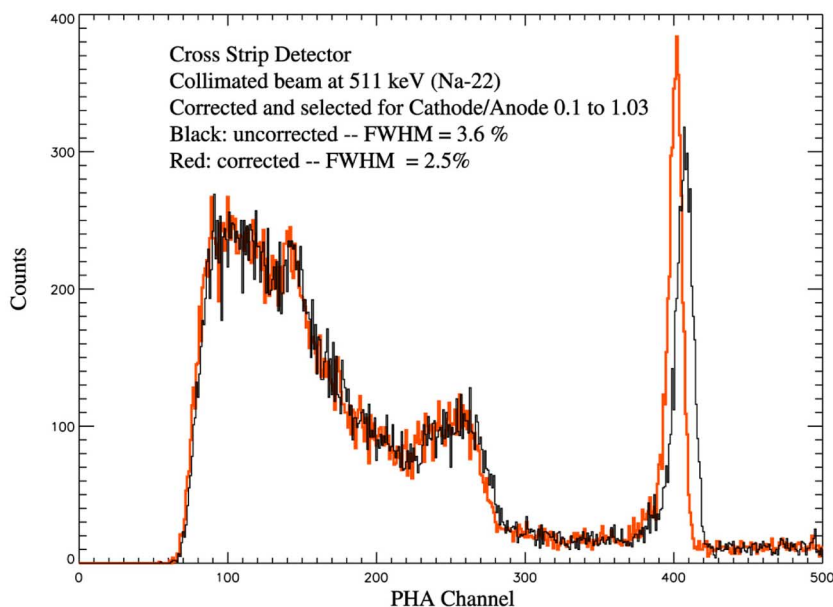
Fig. 19. *^{22}Na 511 keV flood energy spectra (black) before and (red) after pulse height corrections as measured from a group of adjacent anode strips from a prototype cross-strip CZT array. The pulse height corrections compensate for depth-dependent charge attenuation using the cathode/anode pulse height ratio, which is available in real-time to the detector. The resolution of the 511 keV photopeak in the corrected spectrum is 2.5% FWHM. Standard scintillation-based PET detectors have an order of magnitude worse energy resolution.*
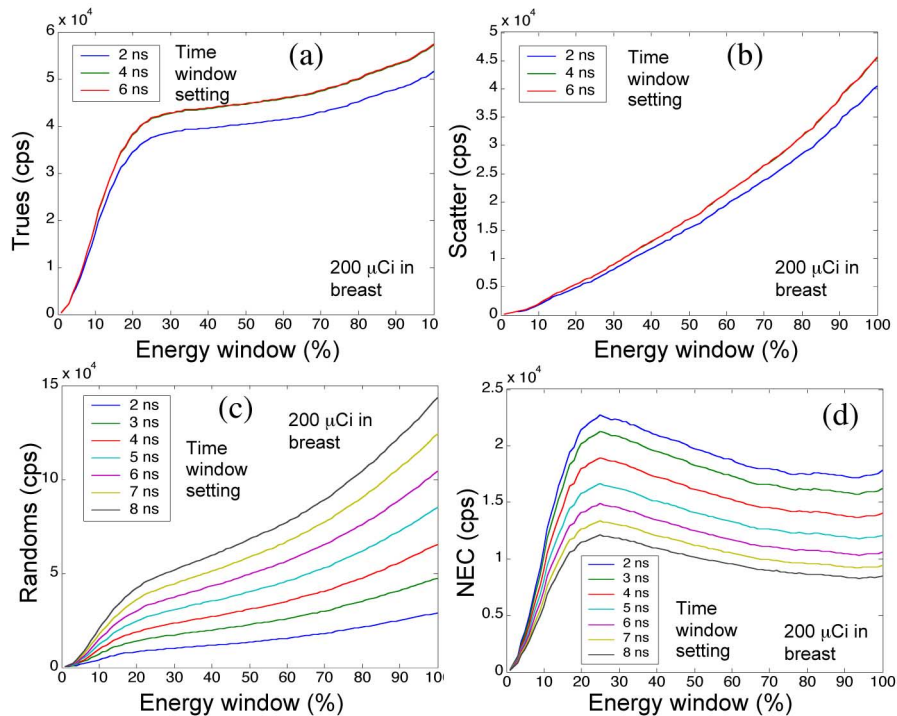
Fig. 20. *Simulated (a) true, (b) scatter, (c) random, and (d) NEC coincidence rates as a function of energy window settings for different coincident time window settings for a simulated acquisition of a breast/body phantom in a LSO-PSAPD dual-panel breast dedicated PET system with an 8 cm detector plate separation with 200 μCi in breast compartment [73]. The excellent energy resolution (≤ 12% FWHM) means a high fraction of good counts are placed in a narrower energy window. A narrower energy window setting helps to significantly reduce both random and scatter background counts. Note that the 4 and 6 ns setting data in the upper left plot cannot be distinguished and appear as one curve.*

is ideal (Fig. 20). However, due to a relatively high random coincidence rate, the peak NEC, which takes into account effects of both the scatter and random coincidence rate on image SNR, is observed at a 2 ns setting for the particular breast imaging phantom configuration simulated [73].

As seen in Fig. 20, the effects of randoms can also be reduced by applying a narrow energy window to reject single photons that have scattered and which would normally contribute to the random coincidence rate. Since the random photon coincidence rate depends upon the square of the detected single photon rates, we expect a narrow energy window can be quite helpful to reduce randoms.

Fig. 21 shows results from simulating a rat size phantom in a PET system built from the high-resolution CZT detectors described in the previous section. Since CZT detector signal formation relies on the propagation of charge, rather than light, the coincidence time resolution is much worse for CZT than is achieved with scintillation detectors. FWHM coincidence time resolution of 8 ns measured in experiments [47] was assumed in the simulations. However, due to the superior energy resolution and very narrow energy window setting (e.g., 6% or 496–526 keV), the random coincidence rate for the rat phantom is low and a relatively high peak NEC is achieved,
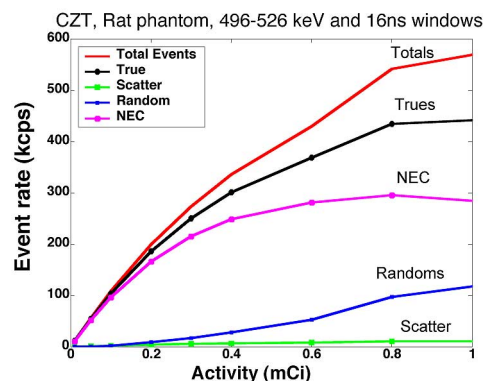
Fig. 21. *Coincident rates calculated from Monte Carlo simulated PET acquisitions in a CZT for a rat phantom (6-cm-diameter 15-cm-long cylinder filled uniformly with ^{18}F activity). For CZT, the energy resolution and window setting used were 3% FWHM at 511 keV and 6% (496–526 keV), respectively, and the coincident time resolution and window used were 8 and 16 ns, respectively. Due to exceptional energy resolution, a narrow energy window can be used to mitigate both scatter and random background counts while preserving high photopeak counts. Hence, absolute true, total, and NEC rates are relatively high and randoms/trues and scatters/trues fractions relatively low for the proposed CZT system.*

even though the coincidence time window setting used is quite large (16 ns).

3) Time-of-Flight (TOF) PET: Due to the recent development of high-Z, high-density inorganic scintillation crystals that also yield sub-nanosecond time resolution, there has been renewed interest in the concept of TOF-PET [74]. This excellent coincidence time resolution allows one to constrain each event and subsequent line projections performed during image reconstruction to a smaller region along each LOR. This constraint improves the SNR via the signal-to-background ratio in the image reconstruction process. The FWHM of the constrained line projection is given by $\Delta l = c \cdot T_r/2$ [74], where c is the speed of light and T_r is the FWHM coincidence time resolution. For example, if $T_r = 500$ ps FWHM, then the line projection is spread (Gaussian distribution) with FWHM = 7.5 cm centered on the estimated emission point. Such a TOF resolution does not itself provide adequate spatial resolution to void the need for the forward and backward line projection reconstruction methods; however, the constraint does facilitate improvements in SNR. The contrast improvement from TOF along any LOR is roughly equal to the square root of the ratio of the subject thickness along that line to the FWHM of the constrained line projection [74]. Thus, there is significant SNR improvement for imaging the trunk of the human body, perhaps a factor of two to five, depending upon the subject size. However, for small animal or dedicated organ imaging such as breast imaging, with the coincidence time resolution of current TOF-PET detector technologies, there is no SNR improvement available since the size of the object under study is on the order of the size of the TOF line constraint (e.g., < 8 cm).

D. Readout Electronics Challenges

The LSO-PSAPD and CZT detectors under investigation for the development of 1 mm resolution PET systems are capable of recording the 3-D photon interaction coordinates [47]–[49], [55], [56], [73], but the main drawback is that there are thousands of electronic channels required [75], [76]. For example, a dual-panel breast-dedicated detector system under development will have more than 20 000 individual readout channels [76]. The $8 \times 8 \times 8$ cm^3 FOV box-shaped CZT system (depicted in Fig. 16) [47], [49] will require more than 9000 channels. The lower gain of semiconductor devices prevents extensive multiplexing of the electronic readout in order to reduce the number of required channels. Thus, a key bottleneck in the development of a PET system built from high-resolution 3-D positioning detectors is the development of application-specific integrated circuits (ASICs) that read out hundreds to thousands of densely packed detector channels with complex event hit patterns [66], [67], [75]–[77].

Fortunately, there are a number of companies as well as national laboratories that have developed such ASICs [75], [76], [78]. For example, NOVA R&D, Inc. (Riverside, CA) has developed a 36-channel charge-sensitive readout ASIC known as RENA-3 [79] [see Fig. 22(a)] for high-sensitivity low-noise high-density readout of semiconductor detectors. A block diagram of the RENA-3 chip is shown in Fig. 22(b). Each of the 36 channels has a charge-sensing preamplifier, Gaussian shaping amplifier, trigger, fast time-stamp circuitry, parallel sample-and-hold, and capability for complex hit pattern readout. Experiments show that the RENA-3 ASIC can handle the spatial, spectral, and temporal requirements for high-performance PET [76].

An example architecture of a data acquisition system built from the RENA-3 is depicted in Fig. 22(c) [76]. A module containing several detectors connects to a readout card. Each readout card comprises three separate PCB boards connected with high-density connectors. The first board is a discrete array of components that are needed to AC couple the high- and low-voltage signals from the detectors into the RENA-3 readout board. The second board in the readout chain comprises many RENA-3 ASICs. The third PCB board in the readout chain is an analog-to-digital sampling and digital processing board. The RENA-3 ASICs are multiplexed into relatively few readout analog-to-digital-converters with field-programmable gate arrays (FPGA) that provide the hit control and sampling logic for the RENA-3 ASICs. These FPGAs forward the hits up to a top-level backplane digital processing board that forms packs of coincidence events into buffers to be transferred to a storage PC over a high-speed optical link.

E. Image Reconstruction Challenges

1) Computational Challenges: Three-dimensional positioning detectors provide additional photon depth positioning bins. The first benefit of this is the capability of photon interaction depth resolution, which mitigates parallax positioning errors and facilitates uniform spatial resolution (see Section II-A3). Another consequence of these advancements would be that the number of system LORs or, alternately, the number of nonzero elements in the system response matrix is increased by orders of magnitude. For example, we are building two 1-mm resolution PET systems, one for breast [48], [73] and the other for small animal imaging [47], [49], with directly measured photon DOI capability that have 4 and 8 billion LORs, respectively [80], and other such billion-LOR systems have been built (e.g., see [81]). A potential benefit of this third dimension of detector resolution is a higher degree of spatial sampling to help recover high spatial frequency signals, provided that additional sampling is indeed required per the Nyquist–Shannon sampling theorem [82].
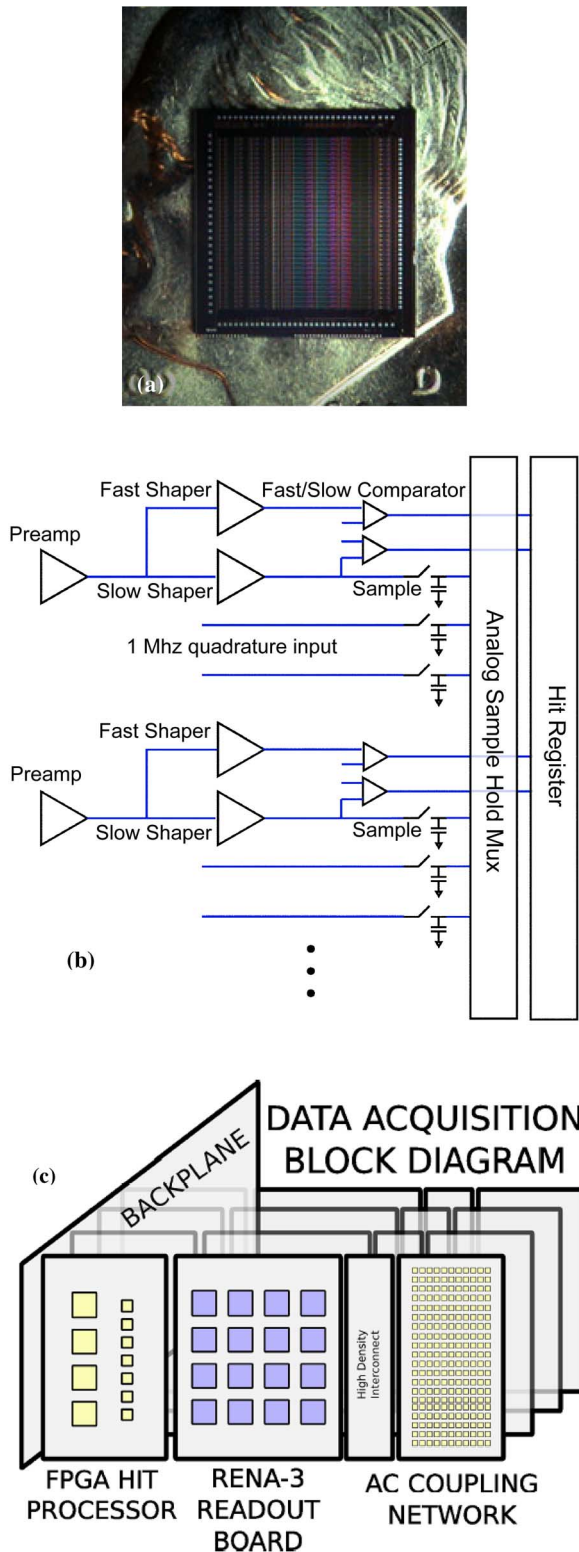
The photon sensitivity of PET systems also continues to increase as the solid angle and detector efficiency of PET systems continue to advance. With increasing photon sensitivity and better SNR, resolution recovery techniques can be used to reconstruct higher resolution images. As a result, the number of image voxels continues to grow at a rate similar to the increase in the number of LORs. It is clear that robust, statistics-based image reconstruction algorithms, ideally with spatially variant response models, are needed to process this mass of data and recover the desired system spatial resolution potential with an acceptable SNR [83].

The desire for improved PET image quality (e.g., spatial resolution, SNR, contrast resolution) and quantitative accuracy (e.g., contrast recovery) has led to a need for more information to be acquired and reconstructed by PET systems and, hence, more complex system matrices and corrections for effects such as scatter to be implemented. Iterative, fully 3-D image reconstruction algorithms that incorporate spatially varying models can improve the quality and quantitative accuracy of image reconstruction for PET [84] at a substantially higher computational and memory cost.

Tissue scatter correction can further improve image quality and accuracy. Running the single scatter correction algorithm requires 2 min on a 3.06 GHz dual processor for data from the GE Advance PET system [85]. This correction must be calculated for every few subset updates and can greatly increase the computational cost of image reconstruction for ultra-high-resolution systems. More accurate multiple scatter techniques require as much as $200\times$ the computation required by the single scatter approximation technique [85]. Further, as the number of LORs and system photon sensitivity increase (enabling higher reconstructed resolution but a greater number of image voxels), the cost of applying accurate system models and scatter correction further increases, preventing a wider use of these techniques to improve image quality and quantification.

2) Processing Algorithms: The computational cost of fully 3-D PET image reconstruction, especially with spatially varying system response models, is daunting. As the number of LORs and reconstructed image resolution continues to increase, the demand for computation power and memory storage for high-resolution PET image reconstruction will continue to explode, in many cases outpacing the advances in processor performance and memory capacity. Algorithms whose complexity does not depend on the number of LORs are attractive to efficiently process the extremely sparse data generated by high-resolution PET systems with minimal memory storage requirements. Three classes of algorithms can help mitigate the problem of the sparseness of the high-resolution 3-D PET data: reduced resolution sinogram binning, 3-D to 2-D rebinning, and list-mode processing.
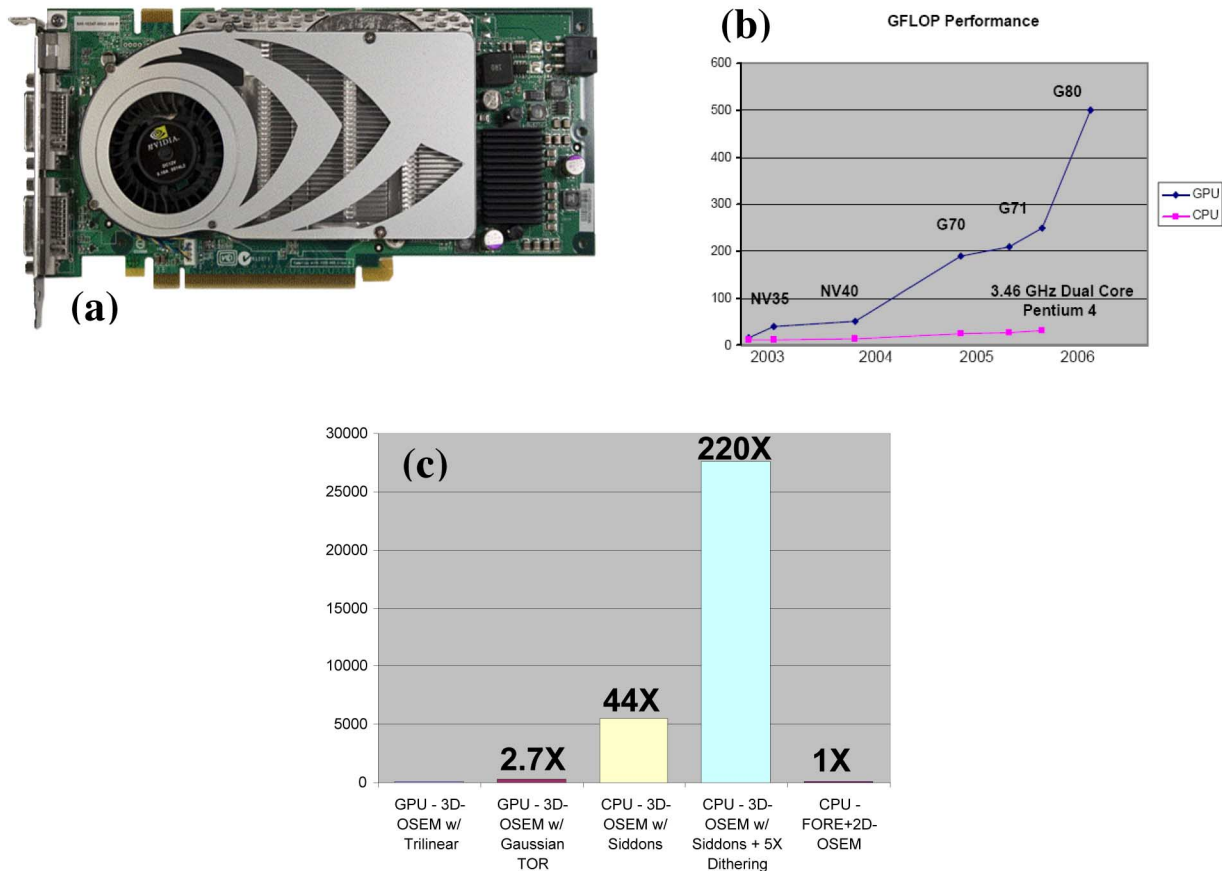
Fig. 23. *(a) The NVIDIA GeForce 7800 GTX GPU (manufactured in 2005, courtesy of NVIDIA Corp.) under investigation for accelerated list-mode 3-D OSEM image reconstruction [80] has a peak performance of more than 200 GFLOPS. (b) Comparison of CPU versus GPU raw performance slope versus time (units of GFLOPS) [98]. (c) CPU versus GPU 3-D OSEM reconstruction time for 50 million events (50 million line projections processed) of a phantom acquired on using the GE Vista DR small animal PET system, [74].*

The process of binning events into a lower resolution sinogram may result in a loss of spatial resolution, since the counts associated with a number of neighboring lines in space that are individually resolvable by the detector system will be accumulated together in the same histogram bin, and this could result in undersampling of the signal [89]. On the other hand, 3-D sinograms that provide sampling of at least twice the Nyquist frequency [82] can be too sparse (i.e., the number of LORs required exceeds or is on the order of the number of events acquired). For one of the 1-mm-resolution PET systems under development with $8 \times 8 \times 8$ cm^3 FOV and six layers of DOI, a 3-D sinogram that samples at the Nyquist frequency requires roughly 80 million bins [80], which is indeed quite sparse. Thus, sinogram binning approaches to deal with sparseness of the data can lead to a tradeoff between desired reconstructed spatial resolution and noise.

Another approach to reduce the effective number of LORs and accelerate image reconstruction is to rebin the 3-D data into a stack of 2-D slices that can be reconstructed independently using a 2-D reconstruction method such as filtered backprojection or 2-D OSEM. Fourier rebinning (FORE) combined with 2-D OSEM [90], [91] is over an order of magnitude faster than fully 3-D OSEM. Furthermore, for whole body clinical scanners, the former has been shown to produce images that are not significantly degraded compared to 3-D OSEM [92]. However, for high-resolution PET systems, the number of counts recorded per LOR is extremely low. As a consequence, the data measured do not accurately reflect the ideal line-integral of the radionuclide activity on which the FORE algorithm relies. Thus, the potential for resolution recovery is lost with this approach [83].

The list-mode processing approach is widely used [93]–[102]. Using list-mode (or histogram) processing, the computation time is independent of the number of LORs in the system and instead is directly proportional to the number of counts in the data set. Since the photon sensitivity of PET systems continues to increase, the

computation time for these processing approaches will also increase. Because GPUs are designed to handle highly parallel geometrical computations, shifting most of the algorithm computations from the CPU to the GPU dramatically accelerates list-mode iterative image reconstruction. The 3-D OSEM algorithm for list-mode data can be formulated as follows [93]:

$$\lambda_j^{m,l} = \frac{\lambda_j^{m,l-1}}{\underbrace{\sum_{i=1}^{I} w_{ii} p_{ij}}_{C}} \underbrace{\sum_{k \in S_i} p_{i_k j} \underbrace{\frac{1}{\sum_{b=1}^{J} p_{i_k b} \lambda_j^{m,l-1}}}_{A}}_{B} \quad (4)$$

where λ_j is the image voxel space, indexed by $j = 1, \ldots, J$. The LOR-space is divided into subsets S_i, $i = 1, \ldots, L$. The current iteration is m and the current subset is l. p_{ij}, the system matrix coefficient, represents the probability for an emission from voxel j to be detected along the LOR i. $\mathbf{A}$ represents the forward projection on the LOR i_k of the current voxel space. $\mathbf{B}$ is the backprojection of every event i_k that goes through voxel j weighted by $1/\mathbf{A}$. $\mathbf{C}$ (via w_{ij}) includes the normalization factors that takes into account the detector efficiency, LOR geometry, and photon tissue attenuation coefficients [93]. The system matrix (p_{ij}) in iterative image reconstruction algorithms models the contribution of each image voxel to each detector pair.

3) Potential for Acceleration: There is thus a great need for fast and memory-efficient line forward and backprojection operations to process these enormous data sets and incorporate spatially varying detector response models and scatter correction techniques. We are studying inexpensive, off-the-shelf graphics processing units (GPUs), a mainstream technology present on graphics cards [80] [see Fig. 23(a)] to greatly accelerate 1) the two most elementary operations of iterative tomographic image reconstruction algorithms, the line backprojection and the line forward projection; and 2) accurate physical system response modeling. Previous GPU implementations of forward and backprojection were limited to sinogram-based data sets without system modeling and performed on the old generation of nonprogrammable GPUs [86], [87]. We are studying the new generation of fully programmable GPUs to support the development of and drastically accelerate advanced image reconstruction algorithms that incorporate an accurate system model and scatter correction to facilitate the highest spatial resolution and quantitative accuracy. Further, we are extending GPU support to include acceleration of list-mode reconstruction for applications such as dynamic PET. The use of GPUs is particularly practical for image reconstruction because most workstations already have a graphics processor for rendering volumetric images.

As of 2007, GPUs are over an order-of-magnitude faster than CPUs [88] [see Fig. 23(b)]. An Intel Pentium IV has a theoretical peak performance of 12 GFLOPS (billion floating-point operations per second); the NVIDIA GeForce 7900GTX GPU (a 2005 technology), shown in Fig. 23(a), has a peak performance of about 200 GFLOPS. GPUs are characterized by extremely high processing parallelism, fast clock-rate, high-bandwidth memory access, and built-in optimized geometrical functions. However, they have quite a limited amount of memory (600 Mb). Nevertheless, these characteristics make them particularly well suited for on-the-fly schemes with low memory profiles and high computational requirements. The highly distributed and parallel architecture has allowed GPU performance to increase at a much faster rate than the CPU [it is commonly said that GPUs follow Moore's law squared; see Fig. 23(b)], and so performance gain measured today between GPUs and CPUs (presently an order of magnitude for a similar priced CPU and GPU) will be even greater in years to come. GPU-based image reconstruction libraries we are developing [80] will continue to exploit GPU performance improvements, which occur much more rapidly than for CPUs [Fig. 23(b)]. In addition, the image reconstruction software under investigation has been carefully designed to be compatible with the standard and well-maintained OpenGL library and the Cg high-level shading programming language of the GPU. These libraries are frequently updated to allow new hardware to function properly. This proposed library will not be bound to specific hardware from a single vendor. GPU-based software will be easily updatable, portable, and maintainable.

Implementation of list-mode 3-D OSEM on the GPU is challenging because the graphics programming interface was not originally designed for general-purpose computation. It turns out that the two main components of list-mode 3-D OSEM (line backprojection and line forward projection) can be reformulated as pseudorendering tasks that can be run extremely efficiently on the GPU [80]. The preliminary implementation of the list-mode 3-D OSEM algorithm on the GPU is more than 40 times faster than a similar implementation on a state-of-the-art CPU [see Fig. 23(c) and Table 4] [80]. For ultra-high-resolution

Table 4 Image Reconstruction Times for Each Case Shown in Fig. 23(c)

Algorithm	Recon. time
CPU 3D-OSEM (Siddon)	5,510 s
CPU 3D-OSEM (Siddon+10X dither.)	55,100 s
GPU 3D-OSEM (Trilinear interp.)	125 s
GPU 3D-OSEM (Gaussian TOR)	340 s
CPU FORE+2D-OSEM	120 s

PET, the size of the system matrix prevents storing it in a lookup table in memory. List-mode on-the-fly computation on the GPU and model simplification are used.

III. SUMMARY AND DISCUSSION

We have discussed a number of technologies we are investigating that, if successful, will each contribute towards improving PET's ability to visualize and quantify low concentrations of a desired signal. In PET-based molecular imaging, the signal arises from the targeting of a radiolabeled probe molecule to cellular and molecular processes occurring within the tissues of the subject under examination. The basic imaging system performance parameters that are under study for enhancement are photon sensitivity, spatial resolution, energy resolution, and coincidence time resolution. Although it is difficult to accurately quantify the resulting molecular sensitivity increase, which is study dependent, we can describe how these performance advances impact the three parameters P, P, and B of equation (1) that directly relate to molecular sensitivity.

A PET system with higher photon sensitivity P allows more signal counts to be positioned per small detector element in a given counting time, enabling higher reconstructed spatial resolution, and thus better statistics to be collected from a smaller ROI volume in the resulting images. Spatial resolution limits how small an ROI volume can be accurately quantified. Excellent spatial resolution allows the use of smaller ROIs to quantify smaller target volumes V_t in order to reject low-frequency background counts while preserving high-frequency signal counts, as well as avoiding spillover of desired signal counts into the background. Finally, a PET system with excellent energy and temporal resolutions allows the use of narrow energy and time window settings to reduce background counts from scatter and random photon contamination while preserving high true signal counts. Measuring lower background counts from scatter and random coincidences facilitates better contrast between signal and background B for visualization of lower concentrations of probe reaching its target. In addition to collecting background signal from scatter and random photons, nonspecific probe targeting also contributes substantially to the total measured background signal B.

With the basic understanding of how PET system performance parameters impact molecular sensitivity, we summarize how the new technologies discussed in this paper will benefit PET performance parameters (e.g., spatial, energy, temporal resolutions, and photon sensitivity).

3-D Positioning Detectors: The use of detectors that can record 3-D coordinates of individual photon interactions in the crystals (e.g., Fig. 12) has several significant benefits for PET performance. Resolution of a third photon interaction coordinate allows one to improve spatial resolution and spatial resolution uniformity throughout the FOV (Section II-A3) (Figs. 11 and 14). It also facilitates the use of relatively thick detectors (~1.8 cm for LSO-PSAPD and ~4.0 cm for CZT) (Section II-B2) (Fig. 12), enabling nearly a factor of two improvement in intrinsic pair coincidence detection efficiency (e.g., 62–74%) and hence overall photon sensitivity compared to designs that use only ~10–12 mm-thick scintillation crystal (~34–40% intrinsic efficiency), without degrading spatial resolution uniformity. This spatial uniformity is also independent of detector bore size so that a smaller system diameter (e.g., 8 cm instead of 20 cm) (Section II-B1) (Fig. 16) may be used to substantially improve P (e.g., from ~3 to 19%, over a factor of six better, for an 8 cm transaxial, 8 cm axial FOV), without affecting spatial resolution and spatial resolution uniformity. Resolving individual photon interactions using 3-D positioning detectors allows more accurate event positioning (Section II-A4), thus enabling improvements in spatial resolution and contrast resolution (Fig. 15) compared to the weighted mean positioning algorithm available to most PET detectors. The availability of 3-D positioning detectors also opens up the possibility of developing signal-processing algorithms capable of including single and tissue-scattered photons into the data set in order to potentially improve reconstructed SNR without compromising spatial resolution or contrast (Section II-B3) (Fig. 18).

Improved Light Collection Efficiency Configuration for a Scintillation Detector Design: The measured light signal in a PET scintillation detector design affects nearly all important PET performance parameters and every effort should be made to design scintillation detectors with the highest light collection efficiency possible. The new scintillation detector readout configuration proposed [e.g., Figs. 6(b) or 8(b)], for 1 mm crystal pixels, yields a light collection efficiency enhancement of roughly a factor of two to five (see Figs. 5 and 7) compared to the conventional end readout [e.g., Figs. 6(a) or 8(a)], with the light signal independent of the photon interaction coordinates (Section II-A2). This high and nonvarying light signal either directly or indirectly impacts spatial, energy, and temporal resolutions as well as photon sensitivity. The magnitude of the available light impacts spatial resolution since most PET scintillation detector designs rely on either light sharing (e.g., [63]) or the multiplexing of the resulting charge created from photodetection (e.g., [64] and [65]) for success of crystal decoding. Thus, a low collected light signal may impact the ability to resolve miniscule crystals in a flood image, resulting in intrinsic spatial resolution degradation.

The light signal also can indirectly affect the photon sensitivity P as well since the smaller the light signal, the fewer pulses detected above a given energy threshold setting above the electronic noise level. Small light signals

can also lead to poor energy resolution. If the energy threshold is set low (i.e., wide energy window setting) to accommodate events with small light pulses and poor photopeak energy resolution, the contribution to B from background scatter and random photons will increase. A robust light signal allows the use of a relatively high energy threshold (narrow energy window setting) to mitigate background photon counts while preserving high photopeak counts (e.g., Fig. 13). The light signal level also affects P via the positioning algorithm for multiplexed detector designs: a higher light signal from a given crystal will weight the positioning of more events toward the correct crystal position. The light signal and its variation from event to event affect both the energy and time resolution, which directly impact B in (1). A factor of two improvement in the energy and time resolution allows the use of a factor of two narrower window setting to reduce background scatter and random counts while maintaining high true photopeak counts.

Poisson statistics of the number of scintillation light photons N created per event contributes only a small fraction (i.e., $\sqrt{N}$) of the observed variation in photopeak pulse height resolution. For example, a 511 keV absorption in high-quality LSO creates roughly 10 000 scintillation photons or a relative variation of $2.35 \cdot \sqrt{10\,000}/10\,000 = 1\%$ FWHM. However, measurements presented in Fig. 13 yielded an average 511 keV photopeak resolution of ~10–11% FWHM, so clearly only a small fraction of the observed energy resolution is due to light photon statistics alone. The observed energy resolution is more likely dominated by non-Poisson effects inherent to the scintillation mechanism.

A significant effect that degrades energy resolution for the standard light readout geometry [Fig. 6(a)] is due to variations in light collection efficiency with varying photon interaction depth. This geometrical effect produces higher light collection efficiency for photon interaction locations closer to the photodetector. The average 511 keV photopeak energy resolution measured for other PET detector designs with ≤ 1 mm crystal pixels is relatively poor > 20% FWHM (e.g., [103], [104]). Note that designs that use fiber coupling of scintillation detectors to photodetectors (e.g., [64] and [104]) suffer from even further light collection losses and variations. The variation of light collection with photon interaction depth within the crystal is not as significant of an issue for the new readout configuration [Fig. 6(b)] since the average path length and number of reflections encountered for light propagating to the photodetector and their variation from event to event are relatively small. Hence an average energy resolution of ~10–11% FWHM at 511 keV rather than > 20% has been observed [54]–[56] (e.g., Fig. 13).

Light collection also affects coincidence time resolution, which is the time resolution for detecting paired coincidence photons. The coincidence time resolution strongly depends upon the variance in arrival time of the signal from the first photoelectron generated in each individual photodetector, which varies linearly with $(\tau/N_e)^2$ [105], where τ is the scintillator decay constant and N_e is the mean number of photoelectrons produced per event in one detector, which in turn depends directly on the average number of scintillation light photons collected (N) as well as the quantum efficiency of the photodetector.

Semiconductor Detectors: The use of semiconductor detectors such as CZT (e.g., Fig. 4) has the advantage of facilitating the development of 3-D photon positioning, ultrahigh intrinsic spatial resolution systems without the complexities of cutting and processing miniscule individual crystal elements (e.g., Fig. 2) (Section II-A1). Another potential benefit of the third dimension of detector resolution is a higher degree of spatial sampling provided, since there would be orders of magnitude more LORs. This could help to recover high spatial frequency signals, if additional sampling is indeed required per the Nyquist–Shannon sampling theorem [82].

Since the ionization signal produced from absorption of an annihilation photon in a semiconductor detector is directly collected (Fig. 3), the electronic SNR is superior, providing excellent energy resolution (Fig. 19) and the ability to use a very narrow energy window to reject scatter and random photon background while maintaining high photopeak counts (photon sensitivity) (Fig. 20). The drawback of worse time resolution due to the slower process of charge transport in a semiconductor detector compared to light transport in a scintillation detector, and its resulting effects on random photon background levels, is offset by this excellent energy resolution. Many single photons contributing to the random rate undergo scatter, which is efficiently mitigated with a narrow energy window (e.g., Figs. 20 and 21). Since neither intercrystal reflectors or photodetectors are required in a semiconductor detector design, the crystal packing fraction is potentially extremely high (> 99%) [e.g., Fig. 12(b)], which facilitates achieving very high photon sensitivity [e.g., ~20% for the $8 \times 8 \times 8$ cm³ FOV CZT design [Fig. 16(b)] with a 496–526 keV energy window] (Section II-B2).

Box-Shaped System Geometry: Since most PET systems use rectangular detector modules, for a fixed transaxial and axial FOV, compared to other detector gantry shapes, a rectangular shape provides the highest photon sensitivity (Section II-B1) (simulated all-interactions data in Fig. 17). The availability of such a system would also allow the design of an adjustable FOV allowing the four side panels to slide very close to the subject contours in order to further increase photon sensitivity.

Highly Integrated Readout Electronics: A new generation of multichannel readout electronics available to efficiently readout densely packed detector channels (Section II-D) (Fig. 22) enables the realization of new PET system designs that utilize novel 3-D position sensitive detector

concepts (e.g., LSO-PSAPD or CZT). This is essential in order to achieve the goal of ultra-high spatial resolution (e.g., $\leq$ 1 mm) in addition to unprecedented photon sensitivity ($\sim$15–20% or 5–7 kcps/μCi) and energy resolution (2–10% FWHM at 511 keV), and good coincident time resolution ($\sim$2–8 ns FWHM) all at once.

Accelerated Fully 3-D Image Reconstruction With Spatially Varying Models: The image reconstruction task for the new generation of ultra-high-resolution high-photon-sensitivity PET systems is a daunting task. The use of list-mode 3-D OSEM and exploitation of powerful GPUs (Section II-E) [Fig. 23(a) and (b)] allows one to realize the complex task of high SNR, ultrahigh spatial resolution image reconstruction with the incorporation of spatially varying models designed to enhance image quality (e.g., spatial resolution, SNR, contrast resolution) and quantitative accuracy (e.g., contrast recovery) in a reasonable time [Fig. 23(c)].

IV. CONCLUSIONS

A. Overall Improvements Expected With the Proposed New Technologies

PET technology has not yet reached its performance potential. There are still substantial improvements to be made in terms of the capability to visualize and quantify small signals emitted from molecular-based diseased processes within a population of cells residing inside a living subject. If successful, the technologies described in this paper will lead to a substantial molecular sensitivity increase. Consider a point-like source of cells emitting signal within the body of a subject and the high-performance CZT PET system (Fig. 16). If one assumes 1) the proposed factor of six improvement in the photon sensitivity P (e.g., 19% versus typically $\leq$ 3%); 2) a factor of three improvement in reconstructed volumetric spatial resolution (e.g., $1 \times 1 \times 1$ mm^3 versus typically $\geq 1.5 \times 1.5 \times 1.5$ mm^3), which enables the measurement of a smaller target volume V_t to reduce background contamination while

preserving a high level of true signal; and 3) a factor of two lower background count rate B via significant reduction in scatter and random photons (e.g., via 3–12% FWHM energy resolution at 511 keV versus typically $\geq$ 20%); then the molecular sensitivity [via (1)] would be enhanced by over an order of magnitude. If achieved, this order of magnitude molecular sensitivity enhancement could, for example, be useful in the clinic to visualize and quantify smaller congregations of malignant cells emitting signal in order to help detect earlier signatures of primary or metastatic cancer. In small animal imaging research, such an advance would be critical to measure lower concentrations of signal associated with new probes, targets, and assays under study. This enhancement would facilitate deeper probes of disease biology within the cells of living subjects and enable quantification of subtle signatures of molecular-based disease processes. It could also help to guide the discovery and development of novel molecular-based treatments. ∎

REFERENCES

[1] R. Haubner, W. A Weber, A. J. Beer *et al.,* "Noninvasive visualization of the activated alpha v beta 3 integrin in cancer patients by positron emission tomography and [F-18]Galacto-RGD," *PLOS Med.,* vol. 2, no. 3, pp. 244–252, Mar. 2005.

[2] A. L Vavere and M. J. Welch, "Preparation, biodistribution, and small animal PET of Ti-45-transferrin," *J. Nucl. Med.,* vol. 46, no. 4, pp. 683–690, Apr. 2005.

[3] P. McQuade, K. E. Martin, T. C. Castle *et al.,* "Investigation into Cu-64-labeled Bis(selenosemicarbazone) and Bis(thiosemicarbazone) complexes as hypoxia imaging agents," *Nucl.*

Med. Biol., vol. 32, no. 2, pp. 147–156, Feb. 2005.

[4] M. K. Robinson, M. Doss, C. Shaller *et al.,* "Quantitative immuno-positron emission tomography imaging oil HER2-positive tumor xenografts with an iodine-124 labeled anti-HER2 diabody," *Cancer Res.,* vol. 65, no. 4, pp. 1471–1478, Feb. 15, 2005.

[5] S. K. Lyons, "Advances in imaging mouse tumour models in vivo," *J. Pathol.,* vol. 205, no. 2, pp. 194–205, Jan. 2005.

[6] C. Waldherr, I. K. Mellinghoff, C. Tran *et al.,* "Monitoring antiproliferative responses to kinase inhibitor therapy in mice with 3 '-deoxy-3 '-F-18-fluorothymidine PET," *J. Nucl. Med.,* vol. 46, no. 1, pp. 114–120, Jan. 2005.

[7] M. L. Thakur, M. R. Aruva, J. Gariepy *et al.,* "PET imaging of oncogene overexpression using Cu-64-vasoactive intestinal peptide (VIP) analog: Comparison with Tc-99m-VIP analog," *J. Nucl. Med.,* vol. 45, no. 8, pp. 1381–1389, Aug. 2004.

[8] A. Aliaga, J. A. Rousseau, R. Ouellette *et al.,* "Breast cancer models to study the expression of estrogen receptors with small animal PET imaging," *Nucl. Med. Biol.,* vol. 31, no. 6, pp. 761–770, Aug. 2004.

[9] H. Barthel, H. Wilson, D. R. Collingridge *et al.,* "In vivo evaluation of [F-18]fluoroetanidazole as a new marker for imaging tumour hypoxia with positron emission tomography," *Br. J. Cancer,* vol. 90, no. 11, pp. 2232–2242, Jun. 1, 2004.

[10] G. Sundaresan, P. J. Yazaki, J. E. Shively *et al.*, "I-124-labeled engineered Anti-CEA minibodies and diabodies allow high-contrast, antigen-specific small-animal PET imaging of xenografts in athymic mice," *J. Nucl. Med.*, vol. 44, no. 12, pp. 1962–1969, Dec. 2003.

[11] B. Solomon, G. A. McArthur, C. Cullinane *et al.*, "Applications of positron emission tomography in the development of molecular targeted cancer therapeutics," *Biodrugs*, vol. 17, no. 5, pp. 339–354, 2003.

[12] H. H. Yang, F. Berger, C. Tran *et al.*, "MicroPET imaging of prostate cancer in LNCAP-SR39TK-GFP mouse xenografts," *Prostate*, vol. 55, no. 1, pp. 39–47, Apr. 1, 2003.

[13] P. Ray, H. Pimenta, R. Paulmurugan, F. Berger, M. E. Phelps, M. Iyer, and S. S. Gambhir, "Noninvasive quantitative imaging of protein-protein interactions in living subjects," *Proc. Nat. Acad. Sci.*, vol. 99, no. 5, pp. 3105–3110, Mar. 5, 2002.

[14] G. D. Luker, V. Sharma, C. M. Pica, J. L. Dahlheimer, W. Li, J. Ochesky, C. E. Ryan, H. Piwnica-Worms, and D. Piwnica-Worms, "Noninvasive imaging of protein-protein interactions in living animals," *Proc. Nat. Acad. Sci.*, vol. 99, no. 10, pp. 6961–6966, May 14, 2002.

[15] N. Adonai, K. N. Nguyen, J. Walsh, M. Iyer, T. Toyokuni, M. E. Phelps, T. McCarthy, D. W. McCarthy, and S. S. Gambhir, "Ex vivo cell labeling with 64Cu-pyruvaldehyde-bis (N4-methylthiosemicarbazone) for imaging cell trafficking in mice with positron-emission tomography," *Proc. Nat. Acad. Sci.*, vol. 99, no. 5, pp. 3030–3035, Mar. 5, 2002.

[16] J. Wang and L. Maurer, "Positron emission tomography: Applications in drug discovery and drug development," *Curr. Topics Med. Chem.*, vol. 5, no. 11, pp. 1053–1075, Sep. 2005.

[17] J. V. Frangioni and R. J. Hajjar, "In vivo tracking of stem cells for clinical trials in cardiovascular disease," *Circulation*, vol. 110, pp. 3378–3383, 2004.

[18] F. Cao, S. Lin, X. Xie, P. Ray, M. Patel, X. Zhang, M. Drukker, S. J. Dylla, A. J. Connolly, X. Chen, I. L. Weissman, S. S. Gambhir, and J. C. Wu, "*In vivo* visualization of embryonic stem cell survival, proliferation, and migration after cardiac delivery," *Circulation*, Feb. 13, 2006.

[19] R. G. Blasberg and J. G. Tjuvajev, "Molecular-genetic imaging: Current and future perspectives," *J. Clin. Invest.*, vol. 111, pp. 1620–1629, 2003.

[20] S. S. Gambhir, "Molecular imaging of cancer with positron emission tomography," *Nature Reviews*, vol. 2, Sep. 2002.

[21] R. Pither, "PET and the role of in vivo molecular imaging in personalized medicine," *Expert Rev. Mol. Diagnost.*, vol. 3, no. 6, pp. 703–713, Nov. 2003.

[22] K. Shah, A. Jacobs, X. O. Breakefield, and R. Weissleder, "Molecular imaging of gene therapy for cancer," *Gene Therapy*, vol. 11, no. 15, pp. 1175–1187, 2004.

[23] G. D. Luker, "Special conference of the american association for cancer research on molecular imaging in cancer: Linking biology, function, and clinical applications in vivo," *Cancer Res.*, vol. 62, pp. 2195–2198, Apr. 1, 2002.

[24] J. C. Wu, M. Inubushi, G. Sundaresan, H. R. Schelbert, and S. S. Gambhir, "Positron emission tomography imaging of cardiac reporter gene expression in living rats," *Circulation*, vol. 106, p. 180, 2002.

[25] A. Jacobs, J. Voges, R. Reszka, M. Lercher, A. Gossmann, L. Kracht, C. Kaestle, R. Wagner, K. Wienhard, and W. Heiss, "Positron-emission tomography of vector-mediated gene expression in gene therapy for gliomas," *Lancet*, vol. 358, no. 9283, pp. 727–729.

[26] M. Inubushi, J. C. Wu, S. S. Gambhir, G. Sundaresan, N. Satyamurthy, M. Namavari, S. Yee, J. R. Barrio, D. Stout, A. F. Chatziioannou, L. Wu, and H. R. Schelbert, "Positron-emission tomography reporter gene expression imaging in rat myocardium," *Circulation*, vol. 107, p. 326, 2003.

[27] D. J. Hnatowich, "Observations on the role of nuclear medicine in molecular imaging," *J. Cell. Biochem.*, vol. 87, no. S39, pp. 18–24.

[28] A. Chakrabarti, K. Zhang, M. R. Aruva, A. W. Opitz, N. J. Wagner, M. L. Thakur, and E. Wickstrom, "Radiohybridization PET imaging of KRAS G12D mRNA expression in human pancreas cancer xenografts with [64Cu]DO3A-peptide nucleic acid-peptide nanoparticles," *Cancer Biol. Therapy*, vol. 6, no. 6, pp. 1–9, Jun. 2007.

[29] M. E. Phelps, S. C. Huang, E. J. Hoffman *et al.*, "An analysis of signal amplification using small detectors in positron emission tomography," *J. Comput. Assist. Tomogr.*, vol. 6, pp. 551–565, 1982.

[30] S. C. Strother, M. E. Casey, and E. J. Hoffman, "Measuring PET scanner sensitivity: Relating count rates to image signal-to-noise ratios using noise equivalent counts," *IEEE Trans. Nucl. Sci.*, vol. 37, pp. 783–788, Apr. 1990.

[31] C. S. Levin, "Primer on molecular imaging technology," *Eur. J. Nucl. Med. Mol. Imag.*, vol. 32, no. 2, pp. S325–S345, Dec. 2005.

[32] S. R. Cherry, Y. Shao, R. W. Silverman *et al.*, "Micro-PET: A high resolution PET scanner for imaging small animals," *IEEE Trans. Nucl. Sci.*, vol. 44, pp. 1161–1166, 1997.

[33] S. Surti, J. S. Karp, A. E. Perkins *et al.*, "Design evaluation of A-PET: A high sensitivity animal PET camera," *IEEE Trans. Nucl. Sci.*, vol. 50, pp. 1357–1363, 2003.

[34] J. Uribe, H. Li, T. Xing *et al.*, "Signal characteristics of individual crystals in high resolution BGO detector designs using PMT-quadrant sharing," *IEEE Trans. Nucl. Sci.*, vol. 50, pp. 355–361, 2003.

[35] R. Fontaine, F. Belanger, J. Cadorette *et al.*, "Architecture of a dual-modality, high-resolution, fully digital positron emission tomography/computed tomography (PET/CT) scanner for small animal imaging," *IEEE Trans. Nucl. Sci.*, vol. 52, pp. 691–696, 2005.

[36] K. Ziemons, E. Auffray, R. Barbier *et al.*, "The ClearPETTM project: Development of a 2nd generation high-performance small animal PET scanner," *Nucl. Instrum. Methods Phys. Res. A*, vol. 537, pp. 307–311, 2005.

[37] Knoxville, TN, Siemens preclinical solutions I. 2007. [Online]. Available: http://www.medical.siemens.com/. Accessed Oct. 2007.

[38] Philips Medical Systems. Andover, MA, 2007. [Online]. Available: http://www.medical.philips.com/main/products/preclinical/. Accessed Oct. 2007.

[39] Gamma Medica-Ideas. Northridge, CA, 2007. [Online]. Available: http://www.gm-ideas.com/. Accessed Oct. 2007.

[40] Ingegneria dei Sistemi Elettronici. Pisa (Italy), 2007. [Online]. Available: http://www.ise-srl.com/YAPPET/. Accessed Oct. 2007.

[41] Raytest GmbH. Straubenhardt (Germany), 2007. [Online]. Available: http://www.raytest.de/. Accessed Oct. 2007.

[42] S. Surti, J. S. Karp, A. E. Perkins *et al.*, "Imaging performance of a-PET: A small animal PET camera," *IEEE Trans. Med. Imaging*, vol. 24, pp. 844–852, 2005.

[43] R. S. Miyaoka, S. G. Kohlmyer, and T. K. Lewellen, "Performance characteristics of micro crystal element (MiCE) detectors," *IEEE Trans. Nucl. Sci.*, vol. 48, pp. 1403–1407, 2001.

[44] Y.-C. Tai, A. Chatziioannou, Y. Yang *et al.*, "Micro-PET II: Design, development and initial performance of an improved microPET scanner for small-animal imaging," *Phys. Med. Biol.*, vol. 48, pp. 1519–1537, 2003.

[45] S. R. Cherry, Y. Shao, M. P. Tornai *et al.*, "Collection of scintillation light from small BGO crystals," *IEEE Trans. Nucl. Sci.*, vol. 42, pp. 1058–1063, 1995.

[46] C. S. Levin and E. J. Hoffman, "Calculation of positron range and its effect on the fundamental limit of positron emission tomography system spatial resolution," *Phys. Med. Biol.*, vol. 44, pp. 781–799, Mar. 1999.

[47] C. S. Levin, J. L. Matteson, R. T. Skelton *et al.*, "Promising characteristics and performance of cadmium zinc telluride detectors for positron emission tomography," presented at the IEEE Nucl. Sci. Symp. Med. Imag. Conf., Rome, Italy, p. 36, Oct. 16–22, 2004, Abstract M2-117, Book of Abstracts, IEEE Nuclear and Plasma Science Society.

[48] C. S. Levin, F. Habte, A. M. K. Foudray, J. Zhang, and G. Chinn, "Impact of high energy resolution detectors on the performance of a PET system dedicated to breast cancer imaging," *Phys. Med.*, vol. 21, pp. 28–34, 2006, suppl. 1.

[49] F. Habte, A. M. K. Foudray, P. D. Olcott, and C. S. Levin, "Effects of system geometry and other physical factors on photon sensitivity of high-resolution positron emission tomography," *Phys. Med. Biol.*, vol. 52, pp. 3753–3772, 2007.

[50] A. Drezet, O. Monnet, F. Mathy *et al.*, "CdZnTe detectors for small field of view positron emission tomographic imaging," *Nucl. Instrum. Methods Phys. Res. A*, vol. 571, no. 1–2, pp. 465–470, Feb. 1, 2007.

[51] K. Ishii, Y. Kikuchi, S. Matsuyama *et al.*, "First achievement of less than 1 mm FWHM resolution in practical semiconductor animal PET scanner," *Nucl. Instrum. Methods Phys. Res. A*, vol. 576, no. 2–3, pp. 435–440, Jun. 2007.

[52] K. R. Slavis, P. Dowkontta, F. Duttweiler, J. W. Epsteina, P. L. Hinka, G. L. Huszar, E. Kalemci, P. C. Leblanc, J. L. Matteson, M. R. Pelling, R. E. Rothschild, E. Stephan, T. O. Tümer, and G. Visser, "2000 Performance of a prototype CdZnTe detector module for hard X-ray astrophysics," in *Proc. SPIE Symp.*, vol. 4140, pp. 249–256.

[53] C. S. Levin, "Design of a high resolution and high sensitivity scintillation crystal array for PET with nearly complete light collection," *IEEE Trans. Nucl. Sci.*, vol. 45, pp. 2236–2243, Oct. 2002.

[54] C. S. Levin, A. M. K. Foudray, P. D. Olcott *et al.*, "Investigation of position sensitive avalanche photodiodes for a new high-resolution PET detector design," *IEEE Trans. Nucl. Sci.*, vol. 51, pp. 805–810, Jun. 2004.

[55] J. Zhang, A. M. K. Foudray, P. D. Olcott, R. Farrell, K. Shah, and C. S. Levin, "Performance characterization of a novel

thin position-sensitive avalanche photodiode for 1 mm resolution positron emission tomography," *IEEE Trans. Nucl. Sci.*, vol. 54, pp. 415–421, Jun. 2007.

[56] A. M. K. Foudray, R. Farrell, P. D. Olcott, K. S. Shah, and C. S. Levin, "Characterization of two thin position-sensitive avalanche photodiodes on a single flex circuit for use in 3-D positioning pet detectors," in *Conf. Rec. 2006 IEEE Nucl. Sci. Symp. Med. Imag.*, pp. 2469–2472.

[57] W. W. Moses, S. E. Derenzo et al., "A room temperature LSO/PIN photodiode PET detector module that measures depth of interaction," *IEEE Trans Nucl. Sci.*, vol. 42–44, pp. 1085–1089, 1995.

[58] P. A. Dokhale, R. W. Silverman, K. S. Shah et al., "Intrinsic spatial resolution and parallax correction using depth-encoding PET detector modules based on position-sensitive APD readout," *IEEE Trans. Nucl. Sci.*, vol. 53, pp. 2666–2670, Oct. 2006.

[59] D. P. McElroy, W. Pimpl, B. J. Pichler et al., "Characterization and readout of MADPET-II detector modules: Validation of a unique design concept for high resolution small animal PET," *IEEE Trans. Nucl. Sci.*, vol. 52, pt. 1, no. 1, pp. 199–204, Feb. 2005.

[60] R. Lecomte, R. A. deKemp, R. Klein et al., "LabPETtm: A second-generation APD-based digital scanner for high-resolution small animal PET imaging," *Med. Phys.*, vol. 33, pp. 2671–2671, Jul. 2006.

[61] R. Grazioso, M. Aykac, M. E. Casey et al., "APD performance in light sharing PET applications," *IEEE Trans. Nucl. Sci.*, vol. 52, pp. 1413–1416, Oct. 2005.

[62] J. L. Matteson, M. R. Pelling, and R. T. Skelton, "CZT detectors with 3-D readout for gamma-ray spectroscopy and imaging," in *Proc. SPIE*, 2002, vol. 4784, pp. 1–13.

[63] M. P. Tornai, G. Germano, and E. Hoffman, "Positioning and energy response of PET block detectors with different light sharing scheme," *IEEE Trans. Nucl. Sci.*, vol. 41, pp. 1458–1463, 1994.

[64] Y. C. Tai, A. Chatziioannou, S. Siegel, J. Young, D. Newport, R. N. Goble, R. E. Nutt, and S. R. Cherry, "Performance evaluation of the microPET P4: A PET system dedicated to animal imaging," *Phys. Med. Biol.*, vol. 46, pp. 1845–1862, 2001.

[65] S. Siegel, R. W. Silverman, S. Yiping, and S. R. Cherry, "Simple charge division readouts for imaging scintillator arrays using a multi-channel PMT," *IEEE Trans. Nucl. Sci.*, vol. 43, pp. 1634–1641, Jun. 1996.

[66] G. Chinn, A. M. K. Foudray, and C. S. Levin, "A method to include single photon events in image reconstruction for a 1 mm resolution PET system built with advanced 3-D positioning detectors," in *Conf. Rec. IEEE Nucl. Sci. Symp. 2006*, Oct. 2006, vol. 3, pp. 1740–1745. IEEE.

[67] G. Chinn, A. M. K. Foudray, and C. S. Levin, "Accurately positioning and incorporating tissue-scattered photons into PET image reconstruction," in *Conf. Rec. IEEE Nucl. Sci. Symp. 2006*, Oct. 2006, vol. 3, pp. 1746–1751.

[68] C. S. Levin, Y.-C. Tai, E. J. Hoffman, M. Dahlbom, and T. H. Farquhar, "Removal of the effect of Compton scattering in 3-D whole body positron emission tomography by Monte Carlo," in *Conf. Rec. IEEE Nucl. Sci. Symp. Med. Imag. 1995*, Oct. 21–28, 1995, vol. 2, pp. 1050–1054.

[69] M. Phelps, *PET: Molecular Imaging and Its Biological Applications.* New York: Springer-Verlag, 2004.

[70] E. J. Hoffman, S. C. Huang, and M. E. Phelps, "Quantitation in positron emission computed tomography: 1. Effect of object size," *J. Comput. Assist. Tomogr.*, vol. 3, pp. 299–308, 1979.

[71] T. R. Degrado, T. G. Turkington, J. J. Williams et al., "Performance-characteristics of a whole-body PET scanner," *J. Nucl. Med.*, vol. 35, no. 8, pp. 1398–1406, Aug. 1994.

[72] G. C. Wang, J. S. Huber, W. W. Moses, W. S. Choong, and J. S. Maltz, "Calibration of a PEM detector with depth of interaction measurement," *IEEE Trans. Nucl. Sci.*, vol. 51, pp. 775–781, Jun. 2004.

[73] J. Zhang, P. D. Olcott, and C. S. Levin, "Evaluation of a dual-head PET camera design dedicated to breast cancer imaging," *Med. Phys.*, vol. 34, no. 2, pp. 689–702, 2007.

[74] T. F. Budinger, "Time-of-flight positron emission tomography: Status relative to conventional," *PET J. Nucl. Med.*, vol. 24, pp. 73–78, 1983.

[75] P. D. Olcott, C. S. Levin, T. Tumer, M. Clajus, V. Cajipe, and S. Hayakawa, "Preliminary results from a front-end readout ASIC for 1 mm resolution PET systems based upon position sensitive avalanche photodiodes," *J. Nucl. Med.*, vol. 47, no. 5, p. 1507, May 2006, suppl.

[76] P. D. Olcott, C. S. Levin, V. Cajipe, M. Clajus, T. Tumer, and A. Volkovskii, "Evaluation of a new readout ASIC for a 1 mm resolution PET system based upon position sensitive avalanche photodiodes," *J. Nucl. Med.*, vol. 48, no. 6, May 2007, Suppl., 135p.

[77] A. M. K. Foudray, G. Chinn, and C. S. Levin, "Incident photon direction calculation using bayesian estimation for high energy photon detector systems with 3d positioning capability," in *Conf. Rec. 2006 IEEE Nucl. Sci. Symp. Med. Imag.*, pp. 208–210.

[78] F. Habte and C. S. Levin, "Study of low noise multichannel readout electronics for high sensitivity PET systems based on avalanche photodiode arrays," *IEEE Trans. Nucl. Sci.*, vol. 51, Jun. 2004.

[79] T. O. Tumer, V. B. Cajipe, M. Clajus, S. Hayakawa, and A. Vokovskii, "Multi-channel front-end readout IC for position sensitive solid-state detectors," in *IEEE Nucl. Sci. Symp. Conf. Rec.*, 2006, no. 1, pp. 384–388.

[80] G. Pratx, G. Chinn, F. Habte, P. Olcott, and C. S. Levin, "Fully-3D list-mode OSEM accelerated by graphics processing units," in *IEEE Nucl. Sci. Symp. Conf. Rec.*, 2006, no. 4, pp. 2196–2202.

[81] M. Rodriguez, W. C. Barker, J. S. Liow, S. Thada, S. Chelikani, T. Mulnix, and R. Carson, "Count rate dependent component-based normalization for the HRRT," *J. Nucl. Med.*, vol. 47, p. 197, 2006, suppl. 1.

[82] R. A. Roberts and B. F. Barton, *Theory of Signal Detectability: Composite Deferred Decision Theory.* Ann Arbor, MI: Univ. of Michigan, 1965.

[83] J. Qi, "High-resolution 3D Bayesian image reconstruction using the microPET small-animal scanner," *Phys. Med. Biol.*, vol. 43, 1998.

[84] A. M. Alession and P. E. Kinahan, "Improved quantitation for PET/CT image

[85] P. J. Markiewicz, M. Tamal, P. J. Julyan, D. L. Hastings, and A. J. Reader, "High accuracy multiple scatter modelling for 3D whole body PET," *Phys. Med. Biol.*, vol. 52, pp. 829–847, 2007.

[86] F. Xu et al., "Accelerating popular tomographic reconstruction algorithms on commodity PC graphics hardware," *IEEE Trans. Nucl. Sci.*, vol. 52, pp. 654–663, Jun. 2005.

[87] B. Cabral et al., "Accelerated volume rendering and tomographic reconstruction using texture mapping hardware," in *Proc. Symp. Vol. Visual.*, 1994, pp. 91–98.

[88] K. Mueller et al., "Why do commodity graphics hardware boards (GPUs) work so well for acceleration of Computed Tomography?" in *Proc. SPIE Electron. Imag. 2007–Comput. Imag. V Keynote*.

[89] R. M. Lewitt and S. Matej, "Overview of methods for image reconstruction from projections in emission coputed tomography," *Proc. IEEE*, vol. 91, Oct. 2003.

[90] M. Defrise, P. Kinahan, D. Townsend, C. Michel, M. Sibomana, and D. Newport, "Exact and approximate rebinning algorithms for 3-D PET data," *IEEE Trans. Med. Imag.*, vol. 16, pp. 145–158, Apr. 1997.

[91] S. Vandenberghe, M. E. Daube-Witherspoon, R. M. Lewitt, and J. S. Karp, "Fast reconstruction of 3D time-of-flight PET data by axial rebinning and transverse mashing," *Phys. Med. Biol.*, vol. 51, pp. 1603–1621, 2006.

[92] X. Liu, C. Comtat, C. Michel, P. Kinahan, M. Defrise, and D. Townsend, "Comparison of 3-D reconstruction with 3d-osem, and with fore+osem for pet," *IEEE Trans. Med. Imag.*, vol. 20, pp. 804–814, Aug. 2001.

[93] A. Rahmim et al., "Statistical list-mode image reconstruction for the high resolution research tomograph," *Phys. Med. Biol.*, vol. 49, pp. 4239–4258, 2004.

[94] A. Rahmim et al., "Statistical dynamic image reconstruction in state-of-the-art high-resolution PET," *Phys. Med. Biol*, vol. 50, 2005.

[95] E. Asma et al., "4D PET image reconstruction from list-mode data," in *Proc. IEEE Nucl. Sci. Symp. Med. Imag. Conf*, 2000.

[96] R. J. Walledge et al., "4D PET with the quad-HIDAC: Development of dynamic list-mode EM image reconstruction," in *Nucl. Sci. Symp. Conf. Rec.*, 2002, IEEE.

[97] R. Huesman, "List-mode maximum-likelihood reconstruction applied to positron emission tomography with irregular sampling," *IEEE Trans. Med. Imag*, vol. 19, pp. 532–537, 2000.

[98] A. Reader, K. Erlandsson, M. Flower, and R. Ott, "Fast accurate iterative reconstruction for low-statistics positron volume imaging," *Phys. Med. Biol.*, vol. 43, pp. 1001–1013, Jul. 1998.

[99] A. Reader, S. Ally, F. Bakatselos, R. Manavaki, R. Walledge, A. Jeavons, P. Julyan, S. Zhao, D. Hastings, and J. Zweit, "One-pass list-mode EM algorithm for high-resolution 3-D PET image reconstruction into large arrays," *IEEE Trans. Nucl. Sci.*, vol. 49, pp. 693–699, 2002.

[100] L. Parra and H. Barrett, "List-mode likelihood: EM algorithm and image quality estimation demonstrated on 2-D PET," *IEEE Trans. Med. Imag.*, vol. 17, pp. 228–235, 1998.

[101] J. Verhaeghe, Y. D'Asseler, S. Vandenberghe, S. Staelens, R. Van de Walle, and I. Lemahieu, "ML reconstruction from dynamic list-mode PET data using temporal splines," in *Nucl. Sci. Symp. Conf. Rec.*, 2004, IEEE.

[102] R. J. Walledge, A. J. Reader, E. O. Aboagye, T. J. Spinks, M. Honer, J. Missimer, and A. P. Jeavons, "4D PET with the quad-HIDAC: Development of dynamic list-mode EM," in *Nucl. Sci. Symp. Conf. Rec.*, 2002, IEEE.

[103] S. Miyaoka, S. G. Kohlmyer, and T. K. Lewellen, "Performance characteristics of micro crystal element (MiCE) detectors," *IEEE Trans. Nucl. Sci.*, vol. 48, Aug. 2001.

[104] Y. C. Tai, A. F. Chatziioannou, Y. Yang, R. W. Silverman, K. Meadors, S. Siegel, D. F. Newport, J. R. Stickel, and S. R. Cherry, "MicroPET II: Design, development and initial performance of an improved microPET scanner for small-animal imaging," *Phys. Med. Biol.*, vol. 48, pp. 1519–1537, 2003.

[105] R. F. Post and L. I. Schiff, "Statistical limitations on the resolving time of a scintillation counter," *Phys. Rev.*, vol. 80, p. 1113, 1950.

[106] C. S. Levin, M. P. Tornai, S. R. Cherry, L. R. MacDonald, and E. J. Hoffman, "Compton scatter and x-ray crosstalk and the use of very thin intercrystal septa in high resolution PET detectors," *IEEE Trans. Nucl. Sci.*, vol. 44-2, pp. 18–24, 1997.

[107] G. Pratx and C. S. Levin, "Accurately positioning events in a high-resolution PET system that uses 3D CZT detectors," in *Conf. Rec. 2007 IEEE Nucl. Sci. Symp. and Med. Imag.*, 2007, pp. 2660–2664.

[108] G. Chinn and C. S. Levin, "PET image reconstruction with a Bayesian projector for multi-electronic collimation schemes," in *Conf. Rec. 2007 IEEE Nucl. Sci. Symp. and Med. Imag.*, 2007, pp. 2799–2802.

ABOUT THE AUTHOR

Craig S. Levin received the B.S. degree *(summa cum laude)* in physics and mathematics from the University of California, Los Angeles (UCLA) and the M.S., M.Phil., and Ph.D. degrees in particle and nuclear physics from Yale University, New Haven, CT.

He is an Associate Professor of radiology with the Molecular Imaging Program and Division of Nuclear Medicine, Stanford University, Stanford, CA. His duties include research, teaching and directing clinical and preclinical imaging system physics issues. Before Stanford he was an Assistant Professor of radiology and a Nuclear Medicine Physicist with the University of California, San Diego, and its affiliated VA San Diego. He performed his postdoctoral training studies in biomedical physics at UCLA in the Departments of Radiological Sciences and Molecular and Medical Pharmacology under an NIH National Research Service Award. At Stanford, he directs clinical nuclear medicine physics. As a core Member of the Molecular Imaging Program at Stanford (MIPS) and as Codirector of the Center for Innovation in *in vivo* Imaging (SCI3), he directs preclinical molecular imaging physics efforts. He is also an affiliated Faculty Member of the Department of Bioengineering as well as Stanford's Bio-X Program, Comprehensive Cancer Center, Cardiovascular Institute, and Biophysics Program. The focus of his research is on the development of novel instrumentation and algorithms for clinical and small animal radionuclide imaging, with a special emphasis on high-resolution positron emission tomography. This research has been supported by grants from the National Institutes of Health (NIH), State of California, Whitaker Foundation, and Susan Komen Foundation. His work has resulted in more than 50 peer-reviewed scientific publications and six U.S. patents. He directs and organizes the annual Small Animal Imaging Workshop at Stanford as well as the biennial international Workshop on the Nuclear Radiology of Breast Cancer.

Dr. Levin is an Associate Editor of the IEEE TRANSACTIONS ON NUCLEAR SCIENCE AND MEDICAL PHYSICS and a Reviewer for the TRANSACTIONS ON MEDICAL IMAGING. He is a reviewer of several prominent scientific journals, including the *Journal of Nuclear Medicine* and *Physics in Medicine and Biology*.